

Brain and Lung Cross-Protection against Ancestral or Emerging SARS-CoV-2 by Intranasal Lentiviral Vaccination in a New hACE2 Transgenic Murine Model

Min-Wen Ku

Pasteur-Theravectys

Pierre Authié

Pasteur-Theravectys

Maryline Bourgine

Institut Pasteur

François Anna

Pasteur-TheraVectys

Amandine Noirat

Pasteur-TheraVectys

Fanny Moncoq

Pasteur-TheraVectys

Benjamin Vesin

Pasteur-TheraVectys

Fabien Nevo

Pasteur-TheraVectys

Jodie Lopez

Institut Pasteur

Philippe Souque

Institut Pasteur <https://orcid.org/0000-0002-3018-5603>

Catherine Blanc

Institut Pasteur <https://orcid.org/0000-0003-4214-1381>

Ingrid Fert

Pasteur-Theravectys

Sébastien Chardenoux

Institut Pasteur

Ilta Lafosse

Institut Pasteur

Delphine Cussigh

Institut Pasteur

David Hardy

Institut Pasteur

Kirill Nemirov

Pasteur-TheraVectys

Françoise Guinet Guinet

Institut Pasteur

Francina Langa Vives

Institut Pasteur

Laleh Majlessi (✉ laleh.majlessi@pasteur.fr)

Institut Pasteur <https://orcid.org/0000-0001-8648-4058>

Pierre Charneau

Institut Pasteur

Article

Keywords: SARS-CoV-2 emerging variants, lentiviral vectors, beta-coronavirus, pre-fusion spike glycoprotein, intranasal vaccination, mucosal immunity, lung inflammation, brain inflammation, central nervous system, olfactory bulb, hACE2 transgenic mice, T-cell immunity

Posted Date: April 12th, 2021

DOI: <https://doi.org/10.21203/rs.3.rs-415309/v1>

License: © ⓘ This work is licensed under a Creative Commons Attribution 4.0 International License.

[Read Full License](#)

1 **Brain and Lung Cross-Protection against Ancestral or Emerging SARS-CoV-2 by Intranasal**
2 **Lentiviral Vaccination in a New hACE2 Transgenic Murine Model**

3

4 Min-Wen Ku^{1,‡}, Pierre Authié^{1,‡}, Maryline Bourguine^{1,‡}, François Anna^{1,‡}, Amandine Noirat¹, Fanny
5 Moncoq¹, Benjamin Vesin¹, Fabien Nevo¹, Jodie Lopez¹, Philippe Souque¹, Catherine Blanc¹, Ingrid Fert¹,
6 Sébastien Chardenoux², Ilta Lafosse², Delphine Cussigh², David Hardy³, Kirill Nemirov¹, Françoise
7 Guinet⁴, Francina Langa Vives², Laleh Majlessi^{1,§,*} and Pierre Charneau^{1,§,*}

8

9 ¹ Institut Pasteur-TheraVectys Joint Lab, Virology Department, 28 rue du Dr. Roux, Paris F-75015, France

0 ² Plate-Forme Centre d'Ingénierie Génétique Murine CIGM, Institut Pasteur

1 ³ Experimental Neuropathology Unit, Institut Pasteur, 28 rue du Dr. Roux, Paris F-75015, France

2 ⁴ Lymphocytes and Immunity Unit, Immunology Department, Institut Pasteur

3

4 [‡]These authors contributed equally

5 [§]Senior authors

6 ^{*}Corresponding authors: (laleh.majlessi@pasteur.fr, pierre.charneau@pasteur.fr)

7 **Abstract (149 words)**

8 COVID-19 vaccines already in use or in clinical development may have reduced efficacy against
9 emerging SARS-CoV-2 variants. Although the neurotropism of SARS-CoV-2 is well established, the
0 vaccine strategies currently developed have not taken into account the protection of the central nervous
1 system. Here, we generated a transgenic mouse strain expressing the human Angiotensin Converting
2 Enzyme 2, with unprecedented brain as well as lung permissibility to SARS-CoV-2 replication. Using this
3 stringent transgenic model, we demonstrated that a non-integrative lentiviral vector, encoding for the spike
4 glycoprotein of the ancestral Wuhan SARS-CoV-2, used in intramuscular prime and intranasal boost elicits
5 sterilizing protection of lung and brain against both the Wuhan and the most genetically distant Manaus P.1
6 SARS-CoV-2 variants. Beyond the induction of strong neutralizing antibodies, the mechanism underlying
7 this broad protection spectrum involves a robust protective spike-specific CD8⁺ T-cell immunity,
8 unaffected by the recent mutations accumulated in the emerging SARS-CoV-2 variants.

9

0

1

2 **Keywords**

3 SARS-CoV-2 emerging variants, lentiviral vectors; beta-coronavirus; pre-fusion spike glycoprotein;
4 intranasal vaccination; mucosal immunity; lung inflammation; brain inflammation; central nervous system;
5 olfactory bulb; hACE2 transgenic mice, T-cell immunity.

6 Introduction

7 Prolongation of the worldwide pandemic coronavirus disease 2019 (COVID-19) requires the
8 development of effective and safe prophylactic second generation vaccines against the Severe Acute
9 Respiratory Syndrome beta-coronavirus 2 (SARS-CoV-2). Although lung is the organ of predilection for
0 SARS-CoV-2, its neurotropism, similar to that of SARS-CoV and Middle East Respiratory Syndrome
1 (MERS)-CoV^{1, 2, 3} has been reported^{4, 5, 6, 7, 8, 9, 10, 11}. Moreover, expression of ACE2 in neuronal and glial
2 cells has been described, making the brain susceptible to neuroinvasion^{12, 13}. Accordingly, COVID-19
3 human patients can present non-specific neurological symptoms such as headache and myalgia, and specific
4 neurological symptoms including anosmia, dysgeusia, impaired consciousness and acute cerebrovascular
5 disease^{6, 14, 15}. Analysis of autopsies of COVID-19 deceased patients demonstrated the presence of SARS-
6 CoV-2 in nasopharynx and brain, and virus entry into the central nervous system (CNS) via the neural-
7 mucosal interface of olfactory mucosa¹⁶. These observations align with the previous report of viruses
8 capable of gaining access to the brain through neural dissemination or hematogenous route¹⁷. Therefore, it
9 is critical to focus on the protective properties of COVID-19 vaccine candidates, not only in the respiratory
0 tract, but also in the brain.

1 New variants of SARS-CoV-2 resulting from mutations accumulating in the envelop spike glycoprotein
2 of SARS-CoV-2 (S_{CoV-2}) have been identified by genome sequencing in diverse geographical locations
3 throughout the world. S_{CoV-2} is composed of S1 and S2 subunits. The former harbors a Receptor Binding
4 Domain (RBD) that encompasses the Receptor Binding Motif (RBM), which is the main functional motif
5 interacting with human Angiotensin Converting Enzyme 2 (hACE2)^{18, 19}. RBD and RBM are prone to
6 mutations that can further improve the fitness of S_{CoV-2} for binding to hACE2. A crucial consideration for
7 such mutations is the alteration in RBD/RBM B-cell epitopes, which can lead to the escape of SARS-CoV-
8 2 variants from the action of neutralizing antibodies (NAbs) raised in individuals previously infected with
9 ancestral SARS-CoV-2 or immunized with S_{CoV-2} -based vaccines. In October-December 2020, B.1.1.7,
0 B.1.351 and P.1 variants have been respectively identified in the UK, South Africa and Manaus (Brazil),
1 with the latter being the most genetically distant²⁰.

2 We have recently established the high performance of a non-integrative lentiviral vector (NILV)
3 encoding the full-length sequence of S_{CoV-2} of the ancestral Wuhan strain when used in systemic prime
4 followed by intranasal (i.n.) boost²¹. LVs allow transgene insertion up to 5 kb in length and offer
5 outstanding potential for gene transfer to the nuclei of host cells^{22, 23, 24, 25}. LVs display *in vivo* tropism for
6 immune cells, notably dendritic cells²⁶. They are non-replicative, non-cytopathic and scarcely
7 inflammatory²⁷. These vectors induce long-lasting B- and T-cell immunity^{22, 23, 24, 25}. LVs are pseudo-
8 typed with the surface glycoprotein of Vesicular Stomatitis Virus, to which the human population has
9 limited exposure. This prevents these vectors from being targeted by preexisting immunity in humans,

0 unlike adenoviral vectors of human serotypes^{28,29}. The safety of LV has been established in humans in a
1 phase I/II Human Immunodeficiency Virus (HIV)-1 vaccine trial (2011-006260-52 EN).

2 Here, we generated new hACE2 transgenic mice with unprecedented brain permissibility to SARS-CoV-
3 2 replication resulting in marked brain inflammation and lethality following infection. They are also prone
4 to SARS-CoV-2 infection in the lung, yet with milder inflammation than in the brain. Using this stringent
5 preclinical animal model, we demonstrated the capability of i.m.-i.n. prime-boost immunization with our
6 NILV-based vaccine candidate to reach full protection of both lungs and CNS against SARS-CoV-2
7 infection. Importantly, the NILV encoding for the spike protein of the ancestral Wuhan SARS-CoV-2
8 induced sterilizing prophylaxis of lung and brain against both the ancestral Wuhan and the most genetically
9 distant P.1 Manaus SARS-CoV-2 variants. Beside the induction of strong neutralizing antibodies (NAbs),
0 the mechanism underlying this protection is linked to a strong poly-specific CD8⁺ T-cell immunity, not
1 affected by the mutations accumulated in the spike protein of the emerging SARS-CoV-2 variants.

2

3 Results

4 Generation of new hACE2 transgenic mice with high brain permissibility to SARS-CoV-2 5 replication

6 To set up a mouse model permissive to SARS-CoV-2 replication allowing assessment of our vaccine
7 candidates, based on the previously produced B6.K18-ACE2^{2PrImn/JAX} mice³⁰, we generated C57BL/6
8 transgenic mice with a LV³¹ carrying the *hACE2* gene under the human cytokeratin 18 promoter, namely
9 “B6.K18-hACE2^{IP-THV}”. The permissibility of these mice to SARS-CoV-2 replication was evaluated after
0 one generation backcross to WT C57BL/6 (N1). N1 mice with varying number of *hACE2* transgene copies
1 per genome (Figure 1A) were sampled and inoculated i.n. with the ancestral Wuhan SARS-CoV-2 (Figure
2 1B). At 3 dpi, the mean \pm SD of lung viral loads was as high as $(3.3 \pm 1.6) \times 10^{10}$ copies of SARS-CoV-2
3 RNA/lung in permissive mice (Figure 1B). SARS-CoV-2 RNA copies per lung $< 1 \times 10^7$ correspond to the
4 genetic material derived from the input in the absence of viral replication²¹. We also noted that the lung
5 viral loads (Figure 1B) were not proportional to the *hACE2* transgene copy number per genome (Figure
6 1A). Remarkably, viral loads as high as $(5.7 \pm 7.1) \times 10^{10}$ copies of SARS-CoV-2 RNA, were also detected
7 in the brain of the permissive mice (Figure 1B). Virus replication/dissemination was also observed,
8 although to a lesser extent, in the heart and kidneys.

9 We further compared the replication of SARS-CoV-2 in lungs and brain and the viral dissemination to
0 various organs in B6.K18-hACE2^{IP-THV} and B6.K18-ACE2^{2PrImn/JAX} mice³⁰ (Figure 1C). The lung viral
1 loads were slightly lower in B6.K18-hACE2^{IP-THV} compared to B6.K18-ACE2^{2PrImn/JAX} mice. However,
2 viral loads in the brain of B6.K18-hACE2^{IP-THV} mice were substantially higher compared to their B6.K18-
3 ACE2^{2PrImn/JAX} counterparts (Figure 1C). Measurement of brain viral loads by Esg qRT-PCR detected $(7.55$
4 $\pm 7.74) \times 10^9$ copies of SARS-CoV-2 RNA in B6.K18-hACE2^{IP-THV} mice and no copies of this replication-
5 related RNA in 4 out of 5 B6.K18-ACE2^{2PrImn/JAX} mice. This dramatic difference of SARS-CoV-2
6 replication in the brain of the two transgenic strains was associated with significantly higher *hACE2* mRNA
7 expression in the brain of B6.K18-hACE2^{IP-THV} mice (Figure 1D). However, *hACE2* mRNA expression in
8 the lungs of B6.K18-hACE2^{IP-THV} mice was also higher than in B6.K18-ACE2^{2PrImn/JAX} mice, despite of the
9 lower viral replication rate in the lungs of the former. A trend towards higher viral loads was also observed
0 in the kidneys and heart of B6.K18-hACE2^{IP-THV} compared to B6.K18-ACE2^{2PrImn/JAX} mice (Figure 1C).

1 In accordance with the lower lung viral loads, as evaluated by qRT-PCR applied to total lung
2 homogenates, B6.K18-hACE2^{IP-THV} mice displayed less pulmonary inflammation than B6.K18-
3 ACE2^{2PrImn/JAX} mice (Figure 1E). Remarkably, this assay applied to total brain homogenates detected
4 substantial degrees of inflammation in B6.K18-hACE2^{IP-THV} — but not in B6.K18-ACE2^{2PrImn/JAX} — mice
5 (Figure 1E). In addition, B6.K18-hACE2^{IP-THV} mice reached the humane endpoint between 3 and 4 dpi and

6 therefore displayed a lethal SARS-CoV-2-mediated disease more rapidly than their B6.K18-ACE2^{2PrImn/JAX}
7 counterparts ³².

8 Therefore, large permissibility to SARS-CoV-2 replication in both lung and CNS, marked brain
9 inflammation and rapid development of a lethal disease are major distinctive features offered by this new
0 B6.K18-hACE2^{IP-THV} transgenic model.

1 **Full protection of lungs and brain in LV::S_{CoV-2}-immunized B6.K18-hACE2^{IP-THV} mice**

2 We generated a LV encoding for the prefusion form of S_{CoV-2} derived from the ancestral Wuhan strain.
3 This prefusion S_{CoV-2} antigen has the Δ675-685 deletion which encompasses the RRAR furin cleavage site
4 in order to limit its conformational dynamics and to maintain better exposure of the S1 B-cell epitopes ³³.
5 For an improved half-life, the sequence also harbors the K^{986P} and V^{987P} consecutive proline substitutions
6 in S2 (Figure S1A) ³⁴. C57BL/6 mice primed (i.m.) and boosted (i.n.) with LVs encoding the wild type or
7 prefusion S_{CoV-2} possessed high serum titers of anti-S_{CoV-2} IgG (Figure S1B), high titers of anti-S_{CoV-2} IgG
8 and IgA in the lung extracts (Figure S1C), and comparable sero-neutralizing activity (Figure S1D). These
9 results indicate that the modifications in the pre-fusion form does not impact positively or negatively its
0 capacity to induce Ab responses against native S_{CoV-2}.

1 We then evaluated the vaccine efficacy of LV::S_{CoV-2} in B6.K18-hACE2^{IP-THV} mice. In a first experiment
2 with these mice, we used an integrative version of the vector. Individuals ($n = 6/\text{group}$) were primed i.m.
3 with 1×10^7 TU/mouse of LV::S_{CoV-2} or an empty LV (sham) at wk 0 and then boosted i.n. at wk 3 with the
4 same dose of the same vectors (Figure 2A). Mice were then challenged with the ancestral Wuhan SARS-
5 CoV-2 at wk 5. A high serum neutralizing activity was detected in LV::S_{CoV-2}-vaccinated mice (Figure 2B).
6 This vaccination conferred complete protection against SARS-CoV-2 replication, not only in the lungs, but
7 also in the brain (Figure 2C). Lung viral load was assessed by a sub-genomic E_{CoV-2} RNA (Esg) qRT-PCR,
8 previously reported to be an indicator of active viral replication ^{35, 36, 37}. Remarkably, quantitation of brain
9 viral loads by Esg qRT-PCR detected no copies of this replication-related SARS-CoV-2 RNA in LV::S_{CoV-2}-
0 vaccinated mice *versus* $(7.55 \pm 7.84) \times 10^9$ copies in the brain of the sham-vaccinated controls.

1 At 3 dpi, cytometric investigation of the lung innate immune cell subsets (Figure 2D, S2A) detected
2 significantly lower proportions of NK (CD11b^{int} NKp46⁺) cells and neutrophils (CD11b⁺ CD24⁺ SiglecF⁻
3 Ly6G⁺) among the lung CD45⁺ cells in the LV::S_{CoV-2}-vaccinated and protected B6.K18-hACE2^{IP-THV}
4 mice, compared to the sham-vaccinated and unprotected controls (Figure 2D). Frequencies of the other
5 lung innate immune cells were not significantly distinct in the protected and unprotected groups (Figure
6 S2B). At 3 dpi, as evaluated by qRT-PCR applied to brain homogenates, LV::S_{CoV-2}-vaccinated B6.K18-
7 hACE2^{IP-THV} mice had significantly lower expression levels of IFN- α , TNF- α , IL-5, IL-6, IL-10, IL-
8 12p40, CCL2, CCL3, CXCL9 and CXCL10, than the sham group (Figure 2E). However, no noticeable

9 changes in lung inflammation could be found between the LV::S_{CoV-2}-vaccinated and sham groups (Figure
0 S2C).

1 Therefore, an i.m.-i.n. prime-boost with ILV::S_{CoV-2} prevents SARS-CoV-2 replication in both lung
2 and CNS anatomical areas and inhibits virus-mediated lung infiltration, as well as neuro-inflammation.

3 **Requirement of i.n. boost for full protection of brain in B6.K18-hACE2^{IP-THV} mice**

4 To go further in the characterization of the protective properties of LV, in the following experiments in
5 B6.K18-hACE2^{IP-THV} mice, we used the safe and non-integrative version of LV. The observed protection
6 of the brain against SARS-CoV-2 may reflect the benefits of the i.n. route of vaccination against this
7 respiratory and neurotropic virus. To address this question, B6.K18-hACE2^{IP-THV} mice were vaccinated
8 with NILV::S_{CoV-2}: (i) i.m. wk 0 and i.n. wk5, as a positive control, (ii) i.n. wk 0, or (iii) i.m. wk 5. Sham-
9 vaccinated controls received i.n. an empty NILV at wks 0 and 5 (Figure 3A). At wk 7, notable proportions
0 of IFN- γ -producing CD8⁺ T cells, specific to several S_{CoV-2} epitopes, were detected in the lungs (Figure 3B)
1 and spleen (Figure S3A top) of NILV::S_{CoV-2}-vaccinated mice. Small numbers of IFN- γ -producing CD4⁺
2 T-cell responses were also detected in the lungs (Figure S3B) and spleen (Figure S3A bottom) of these
3 mice. Higher proportions of lung CD8⁺ T cells with effector memory (Tem) and resident memory (Trm)
4 were detected in the NILV::S_{CoV-2} i.m.-i.n.-vaccinated mice than in their sham counterparts (Figure 3C).

5 Mice were then challenged with SARS-CoV-2 at wk 7 and viral loads were determined in the brain or
6 lungs by E- or Esg- specific qRT-PCR at 3dpi (Figure 3D). In this stringent pre-clinical model a single i.n.
7 or i.m. injection of NILV::S_{CoV-2}, albeit effective, did not induce full protection in all animals of each group.
8 Only i.m. prime followed by i.n. boost conferred full protection of the brain and lungs in all animals,
9 showing the requirement of an i.n. boost to reach full protection. Correlated with the protection levels were
0 the titers of serum and lung anti-S_{CoV-2} IgG and IgA (Figure 3E), as well as the serum SARS-CoV-2
1 neutralizing activity (Figure 3F).

2 On immuno-histological examination, we detected higher numbers of CD3⁺ T cells per mm² of olfactory
3 bulbs of NILV::S_{CoV-2} i.m.-i.n. vaccinated and protected mice than in the sham individuals (Figure 4A). As
4 expected with this LV vaccine, the T-cell response of protected animals was polarized towards the CD8⁺
5 compartment, as evidenced by the higher proportion of CD8⁺ T cells in the olfactory bulbs (Figure 4B) and
6 by the presence of CD8⁺ - but not CD4⁺ - specific reactive T cells in the spleen (Figure S3A). No specifically
7 reacting CD4⁺ T cells was found in the lung either (Figure S3B), and, in the olfactory bulb, CD4⁺ T cells
8 had no distinctive activated or migratory phenotype, as assessed by their surface expression of CD69 or
9 CCR7 (Figure S3C). In line with the absence of CCR7 expression on these T cells, and unlike Murine
0 Hepatitis Virus (MHV) infection³⁸, we saw no up-regulation of CCL19 and CCL21 (CCR7 ligands) in the
1 brain, regardless of the protected status of the mice (Figure S3D). Compared to the NILV::S_{CoV-2} i.m.-i.n.
2 protected group, there were higher amounts of neutrophils (CD11b⁺ Ly6C⁺ Ly6G⁺) in the olfactory bulbs

3 (Figure 4C) and inflammatory monocytes (CD11b⁺ Ly6C⁺ Ly6G⁻) in the brain (Figure 4D) of unprotected
4 mice, as a biomarker of inflammation.

5 Lung histological sections of infected mice detected, at 3 dpi, areas of various size exhibiting mild to
6 moderate interstitial inflammation accompanied by alveolar exudates, peribronchiolar infiltration and
7 minimal to moderate alterations of the bronchiolar epithelium. At this time-point, lesions from the
8 NILV::S_{CoV-2} i.m.-i.n. vaccinated and sham groups did not differ in severity or extension, indicating that
9 the immune arsenal that contributed to virus eradication had not yet been resorbed (Figure S4). Histological
0 examination of brains did not reveal gross alterations of the organ. However, in infected sham-vaccinated
1 mice — but not in their infected NILV::S_{CoV-2} i.m.-i.n.-vaccinated counterparts — periventricular
2 alterations were clearly visible, in the form of infiltrates of predominantly mononuclear leucocytes (Figure
3 4E) or, in one mouse out of three, of a small periventricular hemorrhage (not shown). These alterations
4 were not detected in the vicinity of the meninges.

5 **Complete cross-protection induced by NILV::S_{CoV-2} against the genetically distant P.1 SARS-** 6 **CoV-2 variant**

7 A critical issue regarding the COVID-19 vaccines currently in use is the protective potency against
8 emerging variants. To assess this question with the vaccine candidate developed here, B6.K18-hACE2^{IP-}
9 ^{THV} mice were primed i.m. (wk0) and boosted i.n. (wk5) with NILV::S_{CoV-2} or sham (Figure 5A). Mice were
0 then challenged at wk 7 with SARS-CoV-2 Manaus P.1 strain which is the most genetically distant SARS-
1 CoV-2 variant so far described³⁹. Determination of the brain and lung viral loads at 3dpi demonstrated that
2 i.m.-i.n. prime-boost with NILV encoding the S_{CoV-2} from the ancestral Wuhan sequence induced full
3 protection of the brain and lungs against SARS-CoV-2 Manaus P.1 (Figure 5B).

4 The markedly decreased ability of the sera of NILV::S_{CoV-2}-vaccinated mice to neutralize S_{B1.351} or
5 S_{Manaus P.1} pseudo-viruses, compared to S_{Wuhan}, S_{D614G} or S_{B1.117} pseudo-viruses, (Figure 5C), raised the
6 possibility of T-cell involvement in this total protection. To evaluate this possibility, we vaccinated
7 following the same protocol (Figure 5A), C57BL/6 WT or μ MT KO mice. The latter are deficient in mature
8 B-cell compartment and therefore lack Ig/antibody response⁴⁰. To make these non-transgenic mice
9 permissive to SARS-CoV-2 replication, they were pre-treated 4 days before the SARS-CoV-2 challenge
0 with 3×10^8 IGU of an adenoviral vector serotype 5 encoding hACE2 (Ad5::hACE2)²¹. Determination of
1 lung viral loads at 3 dpi showed complete protection of the lungs in vaccinated WT mice as well as a highly
2 significant protection in vaccinated μ MT KO mice (Figure 5E). This observation determines that B-cell
3 independent and antigen-specific cellular immunity, i.e. T-cell response, plays a remarkable role in LV-
4 mediated protection. This is consistent with the strong CD8⁺ T-cell responses induced by LV::S_{CoV-2} at the
5 systemic level (Figure 5F) and in the lungs (Figure 3B, C), and the recruitment of CD8⁺ T cells in the
6 olfactory bulbs, detectable in vaccinated and challenged mice (Figure 4A, B, Figure 5D). Remarkably, all

7 murine and human CD8⁺ T-cell epitopes identified on S_{CoV-2} Wuhan sequence are preserved in the mutated
8 S_{CoV-2} Manaus P.1 (Table S1). These observations indicate the strong potential of NILV at inducing full
9 protection of lungs and brain against ancestral and emerging SARS-CoV-2 variants by eliciting strong B
0 and T cell-responses. In contrast to the B-cell epitopes which are targets of NAbs²⁰, the so far identified T-
1 cell epitopes have not been impacted by mutations accumulated in the S_{CoV-2} of the emerging variants.

2 Discussion

3 LV-based platforms emerged recently as a powerful vaccination approach against COVID-19, notably
4 when used as a systemic prime followed by mucosal i.n. boost, inducing sterilizing immunity against lung
5 SARS-CoV-2 infection in preclinical animal models ²¹. In the present study, to investigate the efficacy of
6 our vaccine candidates, we generated a new transgenic mouse model, using the LV-based transgenesis
7 approach ⁴¹. The ILV used in this strategy encodes for hACE2 under the control of the cytokeratin K18
8 promoter, i.e., the same promoter as previously used by Perlman's team to generate B6.K18-ACE2^{2PrImn/JAX}
9 mice ³⁰, with a few adaptations to the lentiviral FLAP transfer plasmid. However, the new B6.K18-
0 hACE2^{IP-THV} mice have certain distinctive features, as they express much higher levels of hACE2 mRNA
1 in the brain and display markedly increased brain permissibility to SARS-CoV-2 replication, in parallel
2 with a substantial brain inflammation and development of a lethal disease in <4 days post infection. These
3 distinctive characteristics can arise from differences in the hACE2 expression profile due to: (i) alternative
4 insertion sites of ILV into the chromosome compared to naked DNA, and/or (ii) different effect of the
5 Woodchuck Posttranscriptional Regulatory Element (WPRE) *versus* the alfalfa virus translational enhancer
6 ³⁰, in B6.K18-hACE2^{IP-THV} and B6.K18-ACE2^{2PrImn/JAX} animals, respectively. Other reported *hACE2*
7 humanized mice express the transgene under: (i) murine ACE2 promoter, without reported hACE2 mRNA
8 expression in the brain ⁴², (ii) "hepatocyte nuclear factor-3/forkhead homologue 4" (HFH4) promoter, i.e.,
9 "HFH4-hACE2" C3B6 mice, in which lung is the principal site of infection and pathology ^{43, 44}, and (iii)
0 "CAG" mixed promoter, i.e. "AC70" C3H × C57BL/6 mice, in which hACE2 mRNA is expressed in
1 various organs including lungs and brain ⁴⁵. Comparison of AC70 and B6.K18-hACE2^{IP-THV} mice could
2 yield information to assess the similarities and distinctions of these two models. The B6.K18-hACE2^{IP-THV}
3 murine model not only has broad applications in COVID-19 vaccine studies, but also provides a unique
4 rodent model for exploration of COVID-19-derived neuropathology. Based on the substantial permissibility
5 of the brain to SARS-CoV-2 replication and development of a lethal disease, this pre-clinical model can be
6 considered as even more stringent than the golden hamster model.

7 The source of neurological manifestations associated with COVID-19 in patients with comorbid
8 conditions can be: (i) direct impact of SARS-CoV-2 on CNS, (ii) infection of brain vascular endothelium
9 and, (iii) uncontrolled anti-viral immune reaction inside CNS. ACE2 is expressed in human neurons,
0 astrocytes and oligodendrocytes, located in middle temporal gyrus and posterior cingulate cortex, which
1 may explain the brain permissibility to SARS-CoV-2 in patients ⁴⁶. Previous reports have demonstrated
2 that respiratory viruses can invade the brain through neural dissemination or hematogenous route ¹⁷. Besides
3 that, the direct connection of olfactory system to the CNS via the frontal cortex also represents a plausible
4 route for brain invasion ⁴⁷. Neural transmission of viruses to the CNS can occur as a result of direct neuron
5 invasion through axonal transport in the olfactory mucosa. Subsequent to intraneuronal replication, the
6 virus spreads to synapses and disseminate to anatomical CNS zones receiving olfactory tract projections ⁹,

7 ^{48, 49, 50}. However, the detection of viral RNA in CNS regions without connection with olfactory mucosa
8 suggests the existence of another viral entry into the CNS, including migration of SARS-CoV-2-infected
9 immune cells crossing the hemato-encephalic barrier or direct viral entry pathway via CNS vascular
0 endothelium ¹⁶. Although at steady state, viruses cannot penetrate into the brain through an intact blood-
1 brain barrier ⁴⁸, inflammation mediators which are massively produced during cytokine/chemokine storm,
2 notably TNF- α and CCL2, can disrupt the integrity of blood-brain barrier or increase its permeability,
3 allowing paracellular blood-to-brain transport of the virus or virus-infected leukocytes ^{4, 23}. The use of the
4 highly stringent B6.K18-hACE2^{IP-THV} mice demonstrated the importance of i.n. booster immunization for
5 inducing sterilizing protection of CNS by our LV-based vaccine candidate developed against SARS-CoV-
6 2. Olfactory bulb may control viral CNS infection through the action of local innate and adaptive immunity
7 ⁵¹. In line with these observations, we detected increased frequencies of CD8⁺ T cells at this anatomically
8 strategic area in i.m.-i.n. vaccinated and protected mice. In addition, substantial reduction in the
9 inflammatory mediators was also found in the brain of the i.m.-i.n. vaccinated and protected mice, as well
0 as decreased proportions of neutrophils and inflammatory monocytes respectively in the olfactory bulbs
1 and brain. Regardless of the mechanism of the SARS-CoV-2 entry into the brain, we provide evidence of
2 the full protection of the CNS against SARS-CoV-2 by i.n. booster immunization with NILV::S_{CoV-2}.

3 Importantly, while multiple SARS-CoV-2 variants are emerging around the world, serious questions are
4 being raised about the protection potential of the vaccines currently in use against these variants ²⁰. The
5 NILV::S_{CoV-2} vaccine candidate provides full cross-protection against one of the most genetically distant
6 variants, Manaus P.1, without antigen sequence adaptation. However, existing RNA- or adenoviral-based
7 vaccines showed several folds reduction in neutralizing efficacy of NAbs and protection potential in
8 humans against the new SARS-CoV-2 variants ⁵². Technically, the sequence of the spike can be replaced
9 or adapted easily in all kinds of vaccines. However, switching the spike sequence of new variants for a
0 second or third booster shot can pose the problem of “original sin”. According to this well-documented
1 fact, individuals already vaccinated with the first ancestral S_{CoV-2} sequence, might not be able to mount a
2 new antibody response against the new S_{CoV-2}, but can rather develop a reinforced antibody response against
3 the firstly encountered ancestral S_{CoV-2} ⁵³. It is our belief that the NILV::S_{CoV-2} vaccine candidate remains
4 fully protective against the distant variants contributed by: (i) the high antibody titers with strong
5 neutralizing activity, induced following prime immunization and, (ii) the remarkable capacity of LV to
6 induce strong and long-lasting CD8⁺ T-cell immunity against multiple MHC-I epitopes which are not
7 modified by the mutations so far accumulated in S_{CoV-2} of emerging variants. These two arms of adaptive
8 immunity, strengthened and targeted, by the NILV::S_{CoV-2} i.n. boost, to the principal entry point of the virus
9 efficiently avoid the infection of main anatomical sites, i.e., lungs and brain by generating a mucosal
0 immunity, which is poorly addressed by vaccinal strategies currently deployed.

1 This lack of local immunity can result in a transient presence of SARS-CoV-2 in the respiratory tract,
2 leading to some contagiousness. The partial resistance of the variants to the NAbs generated by the first-
3 generation vaccines may exacerbate this issue in the future, avoiding a complete containment of the
4 outbreak by mass vaccination. The sterilizing protection of the brain and lungs against the ancestral and the
5 most distant variants of SARS-CoV-2 conferred by a i.m.-i.n. prime-boost with NILV::S_{Cov-2} provides a
6 promising COVID-19 vaccine candidate of second generation. This vaccine candidate can be used to induce
7 long-term protection or to broaden the specificity of the protection in previously vaccinated persons or in
8 COVID-19 convalescents against SARS-CoV-2 emerging variants. Protection of the brain, so far not
9 directly addressed by other vaccine strategies, has also to be taken into account, considering the multiple
0 and sometimes severe neuropathological manifestations associated with COVID-19.

1

2 **Methods**

3 **Construction and production of LV**

4 A codon-optimized prefusion S sequence (1-1262) (Table S2) was amplified from pMK-RQ_S-2019-
5 nCoV and inserted into pFlap by restriction/ligation between BamHI and XhoI sites, between the native
6 human ieCMV promoter and a mutated Woodchuck Posttranscriptional Regulatory Element (WPRE)
7 sequence. The *atg* starting codon of WPRE was mutated (mWPRE) to avoid transcription of the
8 downstream truncated “X” protein of Woodchuck Hepatitis Virus for safety concerns (Figure S5). Plasmids
9 were amplified and used to produce LV as previously described ²¹.

0 **Mice**

1 Female C57BL/6JRj mice (Janvier, Le Genest Saint Isle, France) were used between the age of 7 and
2 12 wks. μ MT KO mice were bred at Institut Pasteur animal facilities and were a kind gift of Dr P. Vieira
3 (Institut Pasteur). Transgenic B6.K18-ACE2^{2PrImn/JAX} mice (JAX stock #034860) were from Jackson
4 Laboratories and were a kind gift of Dr J. Jaubert (Institut Pasteur). Transgenic B6.K18-hACE2^{IP-THV} mice
5 were generated and bred, as detailed below, at the CIGM of Institut Pasteur. During the immunization
6 period transgenic mice were housed in individually-ventilated cages under specific pathogen-free
7 conditions. Mice were transferred into individually filtered cages in isolator for SARS-CoV-2 inoculation
8 at the Institut Pasteur animal facilities. Prior to i.n. injections, mice were anesthetized by i.p. injection of
9 Ketamine (Imalgene, 80 mg/kg) and Xylazine (Rompun, 5 mg/kg).

0 **Mouse Transgenesis**

1 The human K18 promoter (GenBank: AF179904.1 nucleotide 90 to 2579) was amplified by nested PCR
2 from A549 cell lysate, as previously described ^{54,55}. The “i6x7” intron (GenBank: AF179904.1 nucleotide
3 2988 to 3740) was synthesized by Genscript. The K18^{JAX} (originally named K18i6x7PA) promoter includes
4 the K18 promoter, the i6x7 intron at 5' and an enhancer/polyadenylation sequence (PA) at 3' of the *hACE2*
5 gene. The K18^{IP-THV} promoter, instead of PA, contains the stronger wild-type WPRE element at 3' of the
6 *hACE2* gene. Unlike the K18^{JAX} construct which harbors the 3' regulatory region containing a polyA
7 sequence, the K18^{IP-THV} construct uses the polyA sequence already present within the 3' Long Terminal
8 Repeats (LTR) of the lentiviral plasmid. The i6x7 intronic part was modified to introduce a consensus 5'
9 splicing donor and a 3' donor site sequence. The AAGGGG donor site was further modified for the
0 AAGTGG consensus site. Based on a consensus sequence logo ⁵⁶, the poly-pyrimidine tract preceding
1 splicing acceptor site (TACAATCCCTC in original sequence GenBank: AF179904.1 and TTTTTTTTTTTT
2 in K18^{JAX}) was replaced by CTTTTTCCTTCC to limit incompatibility with the reverse transcription step
3 during transduction. Moreover, original splicing acceptor site CAGAT was modified to correspond to the
4 consensus sequence CAGGT. As a construction facilitator, a ClaI restriction site was introduced between

5 the promoter and the intron. The construct was inserted into a pFLAP plasmid between the MluI and BamHI
6 sites. *hACE2* gene cDNA was introduced between the BamHI and XhoI sites by restriction/ligation.
7 Integrative LV::K18-hACE2 was produced as described in ²¹ and concentrated by two cycles of
8 ultracentrifugation at 22,000 rpm 1h 4°C.

9 ILV of high titer (4.16×10^9 TU/ml) carrying K18-hACE2^{IP-THV} was used in transgenesis by subzonal
0 micro-injection under the pellucida of fertilized eggs, and transplantation into the pseudo-pregnant
1 B6CBAF1 females. LV allows particularly efficient transfer of the transgene into the nuclei of the fertilized
2 eggs ⁴¹. At N0 generation, $\approx 11\%$ of the mice, i.e., 15 out of 139, had at least one copy of the transgene per
3 genome. Eight N0 *hACE2*⁺ males were crossed with female WT C57BL/6 mice. At N1 generation, $\approx 62\%$
4 of the mice, i.e., 91 out of 147, had at least one copy of the transgene per genome.

5 **Genotyping and quantitation of *hACE2* gene copy number/genome in transgenic mice**

6 Genomic DNA (gDNA) from transgenic mice was prepared from the tail biopsies by phenol-chloroform
7 extraction. Sixty ng of gDNA were used as a template of qPCR with SYBR Green using specific primers
8 listed in Table S3. Using the same template and in the same reaction plate, mouse *pkd1* (Polycystic Kidney
9 Disease 1) and *gapdh* were also quantified. All samples were run in quadruplicate in 10 μ l reaction as
0 follows: 10 min at 95°C, 40 cycles of 15 s at 95°C and 30 sec at 60°C. To calculate the transgene copy
1 number, the $2^{-\Delta\Delta Ct}$ method was applied using the *pkd1* as a calibrator and *gapdh* as an endogenous control.
2 The $2^{-\Delta\Delta Ct}$ provides the fold change in copy number of the *hACE2* gene relative to *pkd1* gene.

3 **Ethical Approval of Animal Studies**

4 Experimentation on mice was realized in accordance with the European and French guidelines (Directive
5 86/609/CEE and Decree 87-848 of 19 October 1987) subsequent to approval by the Institut Pasteur Safety,
6 Animal Care and Use Committee, protocol agreement delivered by local ethical committee (CETEA
7 #DAP20007, CETEA #DAP200058) and Ministry of High Education and Research APAFIS#24627-
8 2020031117362508 v1, APAFIS#28755-2020122110238379 v1.

9 **Humoral and T-cell immunity, Inflammation**

0 As recently detailed elsewhere ²¹, T-splenocyte responses were quantitated by IFN- γ ELISPOT and anti-
1 S IgG or IgA Abs were detected by ELISA by use of recombinant stabilized S_{CoV-2}. NAb quantitation was
2 performed by use of LV particles pseudo-typed with S_{CoV-2} from the diverse variants, as previously
3 described ^{57,58}. The qRT-PCR quantification of inflammatory mediators in the lungs and brain of mice was
4 performed on total RNA extracted by TRIzol reagent, as recently detailed ²¹. CCL19 and CCL21 expression
5 were verified using the following primer pairs: forward primers were 5'-CTG CCT CAG ATT ATC TGC
6 CAT-3' for CCL19 and 5'- AAG GCA GTG ATG GAG GGG-3' for CCL21; reverse primers were 5'-
7 AGG TAG CGG AAG GCT TTC AC -3' for CCL19 and 5'- CGG GGT AAG AAC AGG ATT G -3' for

8 CCL21.

9 **SARS-CoV-2 inoculation**

0 Transgenic B6.K18-hACE2^{IP-THV} or B6.K18-ACE2^{2PrImn/JAX} were anesthetized by i.p. injection of
1 Ketamine and Xylazine mixture, transferred into a level 3 biosafety cabinet and inoculated i.n. with $0.3 \times$
2 10^5 TCID₅₀ of the BetaCoV/France/IDF0372/2020 or Manaus P.1 SARS-CoV-2 clinical isolate ⁵⁹. Mice
3 were inoculated i.n. with 20 μ l of viral inoculum and were housed in an isolator in BioSafety Level 3 animal
4 facilities of Institut Pasteur. The organs recovered from the infected mice were manipulated according to
5 the approved standard procedures of these facilities. Ad5::hACE2 pretreatment of WT of μ MT KO mice
6 before SARS-CoV-2 inoculation was performed as previously described ²¹.

7 **Determination of viral loads in the organs**

8 Organs from mice were removed aseptically and immediately frozen at -80°C. RNA from circulating
9 SARS-CoV-2 was prepared from lungs as recently described ²¹. Briefly, lung homogenates were prepared
0 by thawing and homogenizing of the organs in lysing matrix M (MP Biomedical) with 500 μ l of ice-cold
1 PBS using a MP Biomedical Fastprep 24 Tissue Homogenizer. RNA was extracted from the supernatants
2 of lung homogenates centrifuged during 10 min at 2000g. Missing neutralization step with AVL
3 buffer/carrier RNA here then extraction with Qiagen RNeasy kit These RNA preparations were used to
4 determine viral loads by E-specific qRT-PCR.

5 Alternatively, total RNA was prepared from lungs or other organs using lysing matrix D (MP
6 Biomedical) containing 1 mL of TRIzol reagent and homogenization at 30 s at 6.0 m/s twice using MP
7 Biomedical Fastprep 24 Tissue Homogenizer. Total RNA was extracted using TRIzol reagent
8 (ThermoFisher). These RNA preparations were used to determine viral loads by Esg-specific qRT-PCR,
9 hACE2 expression level or inflammatory mediators.

0 SARS-CoV-2 E gene ⁶⁰ or E sub-genomic mRNA (Esg RNA) ³⁷, was quantitated following reverse
1 transcription and real-time quantitative TaqMan® PCR, using SuperScript™ III Platinum One-Step qRT-
2 PCR System (Invitrogen) and specific primers and probe (Eurofins) (Table S4). The standard curve of Esg
3 mRNA assay was performed using in vitro transcribed RNA derived from PCR fragment of “T7 SARS-
4 CoV-2 Esg mRNA”. The in vitro transcribed RNA was synthesized using T7 RiboMAX Express Large
5 Scale RNA production system (Promega) and purified by phenol/chloroform extraction and two successive
6 precipitations with isopropanol and ethanol. Concentration of RNA was determined by optical density
7 measurement, diluted to 10^9 genome equivalents/ μ L in RNase-free water containing 100 μ g/mL tRNA
8 carrier, and stored at -80°C. Serial dilutions of this in vitro transcribed RNA were prepared in RNase-free
9 water containing 10 μ g/ml tRNA carrier to build a standard curve for each assay. PCR conditions were: (i)
0 reverse transcription at 55°C for 10 min, (ii) enzyme inactivation at 95°C for 3 min, and (iii) 45 cycles of

1 denaturation/amplification at 95°C for 15 s, 58°C for 30 s. PCR products were analyzed on an ABI 7500
2 Fast real-time PCR system (Applied Biosystems).

3 **Cytometric analysis of immune lung and brain cells**

4 Isolation and staining of lung innate immune cells were largely detailed recently ²¹. Cervical lymph
5 nodes, olfactory bulb and brain from each group of mice were pooled and treated with 400 U/ml type IV
6 collagenase and DNase I (Roche) for a 30-minute incubation at 37°C. Cervical lymph nodes and olfactory
7 bulbs were then homogenized with glass homogenizer while brains were homogenized by use of
8 GentleMacs (Miltenyi Biotech). Cell suspensions were then filtered through 100 µm-pore filters, washed
9 and centrifuged at 1200 rpm during 8 minutes. Cell suspensions from brain were enriched in immune cells
0 on Percoll gradient after 25 min centrifugation at 1360 g at RT, without brakes. The recovered cells from
1 lungs were stained as recently described elsewhere ²¹. The recovered cells from brain were stained by
2 appropriate mAb mixture as follows. (i) To detect innate immune cells: Near IR Live/Dead (Invitrogen),
3 FcγII/III receptor blocking anti-CD16/CD32 (BD Biosciences), BV605-anti-CD45 (BD Biosciences), PE-
4 anti-CD11b (eBioscience), PE-Cy7-antiCD11c (eBioscience), (ii) to detect NK, neutrophils, Ly-6C^{+/+}-
5 monocytes and macrophages: Near IR DL (Invitrogen), FcγII/III receptor blocking anti-CD16/CD32 (BD
6 Biosciences), BV605-anti-CD45 (BD Biosciences), PE-anti-CD11b (eBioscience), PE-Cy7-antiCD11c
7 (eBioscience), APC-anti-Ly6G (Miltenyi), BV711-anti-Siglec-F (BD), AF700-anti-NKp46 (BD
8 Biosciences), FITC-anti-Ly6C (ab25025, Abcam) (iii) To detect adaptive immune cells: Near IR Live/Dead
9 (Invitrogen), FcγII/III receptor blocking anti-CD16/CD32 (BD Biosciences), APC-anti-CD45 (BD),
0 PerCP-Cy5.5-anti-CD3 (eBioscience), FITC-anti-CD4 (BD Pharmingen), BV711-anti-CD8 (BD Horizon),
1 BV605-anti-CD69 (Biolegend), PE-anti-CCR7 (eBioscience) and VioBlue-Anti-B220 (Miltenyi), and (iv)
2 to identify lung memory CD8⁺ T-cell subsets: PerCP-Vio700-anti-CD3, BV510-anti-CD8, PE-anti-CD62L,
3 APC-anti-CD69, APC-Cy7-anti-CD44 and FITC-anti-CD103. Cells were incubated with appropriate
4 mixtures for 25 minutes at 4°C, washed in PBS containing 3% FCS and fixed with Paraformaldehyde 4%
5 by an overnight incubation at 4°C. Samples were acquired in an Attune NxT cytometer (Invitrogen) and
6 data analyzed by FlowJo software (Treestar, OR, USA).

7 **Histopathology**

8 Samples from the lungs or brain of transgenic mice were fixed in formalin for 7 days and embedded in
9 paraffin. Paraffin sections (5-µm thick) were stained with Hematoxylin and Eosin (H&E).
0 Histopathological lesions were qualitatively described and when possible scored, using: (i) distribution
1 qualifiers (i.e., focal, multifocal, locally extensive or diffuse), and (ii) a five-scale severity grade, i.e., 1:
2 minimal, 2: mild, 3: moderate, 4: marked and 5: severe.

3

4 References

- 5 1. Glass, W.G., Subbarao, K., Murphy, B. & Murphy, P.M. Mechanisms of host defense following severe acute respiratory
6 syndrome-coronavirus (SARS-CoV) pulmonary infection of mice. *J Immunol* **173**, 4030-4039 (2004).
- 7
8 2. Li, K. *et al.* Middle East Respiratory Syndrome Coronavirus Causes Multiple Organ Damage and Lethal Disease in
9 Mice Transgenic for Human Dipeptidyl Peptidase 4. *J Infect Dis* **213**, 712-722 (2016).
- 0
1 3. Netland, J., Meyerholz, D.K., Moore, S., Cassell, M. & Perlman, S. Severe acute respiratory syndrome coronavirus
2 infection causes neuronal death in the absence of encephalitis in mice transgenic for human ACE2. *J Virol* **82**, 7264-
3 7275 (2008).
- 4
5 4. Aghagoli, G. *et al.* Neurological Involvement in COVID-19 and Potential Mechanisms: A Review. *Neurocrit Care*
6 (2020).
- 7
8 5. Fotuhi, M., Mian, A., Meysami, S. & Raji, C.A. Neurobiology of COVID-19. *J Alzheimers Dis* **76**, 3-19 (2020).
- 9
0 6. Hu, J., Jolkkonen, J. & Zhao, C. Neurotropism of SARS-CoV-2 and its neuropathological alterations: Similarities with
1 other coronaviruses. *Neurosci Biobehav Rev* **119**, 184-193 (2020).
- 2
3 7. Liu, J. *et al.* Longitudinal characteristics of lymphocyte responses and cytokine profiles in the peripheral blood of
4 SARS-CoV-2 infected patients. *EBioMedicine* **55**, 102763 (2020).
- 5
6 8. Politi, L.S., Salsano, E. & Grimaldi, M. Magnetic Resonance Imaging Alteration of the Brain in a Patient With
7 Coronavirus Disease 2019 (COVID-19) and Anosmia. *JAMA Neurol* **77**, 1028-1029 (2020).
- 8
9 9. Roman, G.C. *et al.* The neurology of COVID-19 revisited: A proposal from the Environmental Neurology Specialty
0 Group of the World Federation of Neurology to implement international neurological registries. *J Neurol Sci* **414**,
1 116884 (2020).
- 2
3 10. von Weyhern, C.H., Kaufmann, I., Neff, F. & Kremer, M. Early evidence of pronounced brain involvement in fatal
4 COVID-19 outcomes. *Lancet* **395**, e109 (2020).
- 5
6 11. Whittaker, A., Anson, M. & Harky, A. Neurological Manifestations of COVID-19: A systematic review and current
7 update. *Acta Neurol Scand* **142**, 14-22 (2020).
- 8
9 12. Chen, R. *et al.* The spatial and cell-type distribution of SARS-CoV-2 receptor ACE2 in human and mouse brain. *BioRxiv*
0 (2020).
- 1
2 13. Xu, J. & Lazartigues, E. Expression of ACE2 in Human Neurons Supports the Neuro-Invasive Potential of COVID-19
3 Virus. *Cell Mol Neurobiol* (2020).
- 4
5 14. Bourgonje, A.R. *et al.* Angiotensin-converting enzyme 2 (ACE2), SARS-CoV-2 and the pathophysiology of
6 coronavirus disease 2019 (COVID-19). *J Pathol* **251**, 228-248 (2020).
- 7
8 15. Mao, L. *et al.* Neurologic Manifestations of Hospitalized Patients With Coronavirus Disease 2019 in Wuhan, China.
9 *JAMA Neurol* **77**, 683-690 (2020).
- 0
1 16. Meinhardt, J. *et al.* Olfactory transmucosal SARS-CoV-2 invasion as a port of central nervous system entry in
2 individuals with COVID-19. *Nat Neurosci* (2020).
- 3
4 17. Desforges, M., Le Coupanec, A., Stodola, J.K., Meessen-Pinard, M. & Talbot, P.J. Human coronaviruses: viral and
5 cellular factors involved in neuroinvasiveness and neuropathogenesis. *Virus Res* **194**, 145-158 (2014).
- 6
7 18. Hoffmann, M. *et al.* SARS-CoV-2 Cell Entry Depends on ACE2 and TMPRSS2 and Is Blocked by a Clinically Proven
8 Protease Inhibitor. *Cell* **181**, 271-280 e278 (2020).
- 9
0 19. Shang, J. *et al.* Structural basis of receptor recognition by SARS-CoV-2. *Nature* **581**, 221-224 (2020).
- 1
2 20. Hoffmann, M. *et al.* SARS-CoV-2 variants B.1.351 and P.1 escape from neutralizing antibodies. *Cell* (2021).
- 3
4 21. Ku, M.W. *et al.* Intranasal vaccination with a lentiviral vector protects against SARS-CoV-2 in preclinical animal
5 models. *Cell Host Microbe* **29**, 236-249 e236 (2021).

- 6
7
8
9
0
1
2
3
4
5
6
7
8
9
0
1
2
3
4
5
6
7
8
9
0
1
2
3
4
5
6
7
8
9
0
1
2
3
4
5
6
7
8
9
0
1
2
3
4
5
6
7
8
9
0
1
2
3
4
5
6
7
8
9
0
1
2
3
4
5
6
7
8
9
22. Di Nunzio, F. *et al.* HIV-derived vectors for therapy and vaccination against HIV. *Vaccine* **30**, 2499-2509 (2012).
 23. Hu, B., Tai, A. & Wang, P. Immunization delivered by lentiviral vectors for cancer and infectious diseases. *Immunol Rev* **239**, 45-61 (2011).
 24. Ku, M.W. *et al.* A Single Dose of NILV-Based Vaccine Provides Rapid and Durable Protection against Zika Virus. *Mol Ther.* 2020 May 20;S1525-0016(20)30250-1. doi: 10.1016/j.ymthe.2020.05.016. (2020).
 25. Zennou, V. *et al.* HIV-1 genome nuclear import is mediated by a central DNA flap. *Cell* **101**, 173-185 (2000).
 26. Arce, F., Rowe, H.M., Chain, B., Lopes, L. & Collins, M.K. Lentiviral vectors transduce proliferating dendritic cell precursors leading to persistent antigen presentation and immunization. *Mol Ther* **17**, 1643-1650 (2009).
 27. Lopez, J. *et al.* An Optimized Poly-antigenic Lentiviral Vector Induces Protective CD4+ T-Cell Immunity and Predicts a Booster Vaccine against Mycobacterium tuberculosis. (Submitted).
 28. Rosenberg, S.A. *et al.* Immunizing patients with metastatic melanoma using recombinant adenoviruses encoding MART-1 or gp100 melanoma antigens. *J Natl Cancer Inst* **90**, 1894-1900 (1998).
 29. Schirmbeck, R., Reimann, J., Kochanek, S. & Kreppel, F. The immunogenicity of adenovirus vectors limits the multispecificity of CD8 T-cell responses to vector-encoded transgenic antigens. *Mol Ther* **16**, 1609-1616 (2008).
 30. McCray, P.B., Jr. *et al.* Lethal infection of K18-hACE2 mice infected with severe acute respiratory syndrome coronavirus. *J Virol* **81**, 813-821 (2007).
 31. Nakagawa, T. & Hoogenraad, C.C. Lentiviral transgenesis. *Methods Mol Biol* **693**, 117-142 (2011).
 32. Winkler, E.S. *et al.* SARS-CoV-2 infection of human ACE2-transgenic mice causes severe lung inflammation and impaired function. *Nat Immunol* **21**, 1327-1335 (2020).
 33. McCallum, M., Walls, A.C., Bowen, J.E., Corti, D. & Veessler, D. Structure-guided covalent stabilization of coronavirus spike glycoprotein trimers in the closed conformation. *Nat Struct Mol Biol* **27**, 942-949 (2020).
 34. Walls, A.C. *et al.* Structure, Function, and Antigenicity of the SARS-CoV-2 Spike Glycoprotein. *Cell* **181**, 281-292 e286 (2020).
 35. Chandrashekar, A. *et al.* SARS-CoV-2 infection protects against rechallenge in rhesus macaques. *Science*. May 2020:eabc4776. doi: 10.1126/science.abc4776. PMID: 32434946. (2020).
 36. Tostanoski, L.H. *et al.* Ad26 vaccine protects against SARS-CoV-2 severe clinical disease in hamsters. *Nat Med* **26**, 1694-1700 (2020).
 37. Wolfel, R. *et al.* Virological assessment of hospitalized patients with COVID-2019. *Nature* **581**, 465-469 (2020).
 38. Cupovic, J. *et al.* Central Nervous System Stromal Cells Control Local CD8(+) T Cell Responses during Virus-Induced Neuroinflammation. *Immunity* **44**, 622-633 (2016).
 39. Buss, L.F. *et al.* Three-quarters attack rate of SARS-CoV-2 in the Brazilian Amazon during a largely unmitigated epidemic. *Science* **371**, 288-292 (2021).
 40. Kitamura, D., Roes, J., Kuhn, R. & Rajewsky, K. A B cell-deficient mouse by targeted disruption of the membrane exon of the immunoglobulin mu chain gene. *Nature* **350**, 423-426 (1991).
 41. Nakagawa, T. & Hoogenraad, C.C. Lentiviral transgenesis. *Methods Mol Biol* **693**, 117-142 (2011).
 42. Yang, X.H. *et al.* Mice transgenic for human angiotensin-converting enzyme 2 provide a model for SARS coronavirus infection. *Comp Med* **57**, 450-459 (2007).
 43. Jiang, R.D. *et al.* Pathogenesis of SARS-CoV-2 in Transgenic Mice Expressing Human Angiotensin-Converting Enzyme 2. *Cell* **182**, 50-58 e58 (2020).
 44. Menachery, V.D. *et al.* SARS-like WIV1-CoV poised for human emergence. *Proc Natl Acad Sci U S A* **113**, 3048-3053 (2016).

- 0
1
2
3
4
5
6
7
8
9
0
1
2
3
4
5
6
7
8
9
0
1
2
3
4
5
6
7
8
9
0
1
2
3
4
5
6
45. Tseng, C.T. *et al.* Severe acute respiratory syndrome coronavirus infection of mice transgenic for the human Angiotensin-converting enzyme 2 virus receptor. *J Virol* **81**, 1162-1173 (2007).
 46. Song, E. *et al.* Neuroinvasion of SARS-CoV-2 in human and mouse brain. *bioRxiv* (2020).
 47. Mori, I., Nishiyama, Y., Yokochi, T. & Kimura, Y. Olfactory transmission of neurotropic viruses. *J Neurovirol* **11**, 129-137 (2005).
 48. Berth, S.H., Leopold, P.L. & Morfini, G.N. Virus-induced neuronal dysfunction and degeneration. *Front Biosci (Landmark Ed)* **14**, 5239-5259 (2009).
 49. Koyuncu, O.O., Hogue, I.B. & Enquist, L.W. Virus infections in the nervous system. *Cell Host Microbe* **13**, 379-393 (2013).
 50. Zubair, A.S. *et al.* Neuropathogenesis and Neurologic Manifestations of the Coronaviruses in the Age of Coronavirus Disease 2019: A Review. *JAMA Neurol* **77**, 1018-1027 (2020).
 51. Durrant, D.M., Ghosh, S. & Klein, R.S. The Olfactory Bulb: An Immunosensory Effector Organ during Neurotropic Viral Infections. *ACS Chem Neurosci* **7**, 464-469 (2016).
 52. Moore, J.P. & Offit, P.A. SARS-CoV-2 Vaccines and the Growing Threat of Viral Variants. *JAMA* **325**, 821-822 (2021).
 53. Brown, E.L. & Essigmann, H.T. Original Antigenic Sin: the Downside of Immunological Memory and Implications for COVID-19. *mSphere* **6** (2021).
 54. Chow, Y.H. *et al.* Development of an epithelium-specific expression cassette with human DNA regulatory elements for transgene expression in lung airways. *Proc Natl Acad Sci U S A* **94**, 14695-14700 (1997).
 55. Koehler, D.R. *et al.* A human epithelium-specific vector optimized in rat pneumocytes for lung gene therapy. *Pediatr Res* **48**, 184-190 (2000).
 56. Dogan, R.I., Getoor, L., Wilbur, W.J. & Mount, S.M. Features generated for computational splice-site prediction correspond to functional elements. *BMC Bioinformatics* **8**, 410 (2007).
 57. Anna, F. *et al.* High seroprevalence but short-lived immune response to SARS-CoV-2 infection in Paris. *Eur J Immunol* (2020).
 58. Sterlin, D. *et al.* IgA dominates the early neutralizing antibody response to SARS-CoV-2. *Sci Transl Med* (2020).
 59. Lescure, F.X. *et al.* Clinical and virological data of the first cases of COVID-19 in Europe: a case series. *Lancet Infect Dis* **20**, 697-706 (2020).
 60. Corman, V., Bleicker, T., Brünink, S. & Drosten, C. Diagnostic detection of 2019-nCoV by real-time RT-PCR. <https://www.who.int/docs/default-source/coronaviruse/protocol-v2-1.pdf> (2020).

7 **Acknowledgments**

8 The authors are grateful to Pr S. van der Werf (National Reference Centre for Respiratory Viruses hosted
9 by Institut Pasteur, Paris, France), F. Guivel-Benhassine and Pr O. Schwartz (Institut Pasteur) for providing
0 the BetaCoV/France/IDF0372/2020 and P.1. Manaus SARS-CoV-2 clinical isolates. The strain
1 BetaCoV/France/IDF0372/2020 was supplied through the European Virus Archive goes Global (Evag)
2 platform, a project that has received funding from the European Union's Horizon 2020 research and
3 innovation program under grant agreement No 653316. The authors thank Pr G. Milon for fruitful advice
4 and discussion, Dr H. Mouquet and Dr C. Planchais for providing recombinant homotrimeric S proteins,
5 Dr N. Escriou and Dr M. Gransagne for providing a plasmid containing the prefusion S_{CoV-2} sequence, and
6 M. Tichit for excellent technical assistance in preparing histological sections.

7 This work was supported by the «URGENCE COVID-19» fundraising campaign of Institut Pasteur,
8 TheraVectys and Agence Nationale de la Recherche (ANR) HuMoCID. M.W. Ku is part of the Pasteur -
9 Paris University (PPU) International PhD Program and received funding from the Institut Carnot Pasteur
0 Microbes & Santé, and the European Union's Horizon 2020 research and innovation program under the
1 Marie Skłodowska-Curie grant agreement No 665807.

2 **Author Contributions**

3 Study concept and design: MWK, MB, FA, FLV, LM, PC, acquisition of data: MWK, PA, MB, FA,
4 AN, BV, FN, JL, PS, CB, KN, LM, construction and production of LV and technical support: PA, AN, FM,
5 PS, CB, IF, analysis and interpretation of data: MWK, PA, MB, FA, FG, FLV, LM, PC, mouse transgenesis:
6 SC, IL, DC, FLV, histology: DH, FG, drafting of the manuscript: MWK, PA, LM, PC.

7 **Declaration of Interests**

8 PC is the founder and CSO of TheraVectys. MWK, FA, PA, AN, FM, BV, FN, JL, IF and KN are
9 employees of TheraVectys. Other authors declare no competing interests. MWK, FA, AN, FLV, LM and
0 PC are inventors of a pending patent directed to the B6.K18-hACE2^{IP-THV} transgenic mice and the potential
1 of i.n. NILV::S_{CoV-2} vaccination at protecting brain against SARS-CoV-2.

632 **Figure Legend**

633 **Figure 1. Large permissibility of the lungs and brain of K18-hACE2^{IP-THV} transgenic mice to**
634 **SARS-CoV-2 replication. (A)** Representative genotyping results from 15 N1 B6.K18-hACE2^{IP-THV}
635 mice as performed by qPCR to determine their *hACE2* gene copy number per genome. Dots represent
636 individual mice. **(B)** Phenotyping of the same mice, presented in the same order, inoculated i.n. with
637 0.3×10^5 TCID₅₀ at the age of 5-7 wks and viral loads determination in the indicated organs at 3 dpi
638 by conventional E-specific qRT-PCR. **(C)** Comparative permissibility of various organs from K18-
639 hACE2^{IP-THV} and B6.K18-ACE2^{2PrImn/JAX} transgenic mice to SARS-CoV-2 replication, as determined
640 at 3 dpi by conventional E-specific or sub-genomic Esg-specific qRT-PCR. Red lines indicate the qRT-
641 PCR limits of detection. Statistical significance of the difference was evaluated by Mann-Whitney test
642 (*= $p < 0.01$, **= $p < 0.00$). **(D)** Comparative quantitation of *hACE-2* mRNA in the lungs and brain of
643 B6.K18-hACE2^{IP-THV} and B6.K18-ACE2^{2PrImn/JAX} transgenic mice. **(E)** Heatmap recapitulating log₂
644 fold change in cytokine and chemokine mRNA expression in the lungs or brain of B6.K18-hACE2^{IP-}
645 ^{THV} and B6.K18-ACE2^{2PrImn/JAX} transgenic mice at 3 dpi. Data were normalized versus untreated
646 controls.

647 **Figure 2. Vaccination with LV::S_{CoV-2} protects both lungs and central nervous system from**
648 **SARS-CoV-2 infection in K18-hACE2^{IP-THV} transgenic mice. (A)** Timeline of prime-boost
649 LV::S_{CoV-2} vaccination and SARS-CoV-2 challenge in K18-hACE2^{IP-THV} mice. **(B)** Serum
650 neutralization capacity of anti-S_{CoV-2} Abs in LV::S_{CoV-2}-vaccinated mice. **(C)** Viral loads as determined
651 in various organs at 3dpi by use of conventional E-specific or sub-genomic Esg-specific qRT-PCR.
652 Red lines indicate the qRT-PCR detection limits. Statistical significance of the difference was evaluated
653 by Mann-Whitney test (*= $p < 0.01$, **= $p < 0.001$). **(D)** Cytometric gating strategy determined to
654 identify and quantify lung NK cells and neutrophils in the lungs of LV::S_{CoV-2}- or sham-vaccinated and
655 SARS-CoV-2-challenged K18-hACE2^{IP-THV} transgenic mice at 3 dpi. Percentages of NK and
656 neutrophil subset were calculated versus total lung CD45⁺ cells. **(E)** Relative log₂ fold change in
657 cytokine and chemokine mRNA expression in the brain of LV::S_{CoV-2}- or sham-immunized and SARS-
658 CoV-2-challenged K18-hACE2^{IP-THV} transgenic mice at 3 dpi. Means \pm SD are shown. Data were
659 normalized versus untreated controls. Statistical significance was evaluated by two tailed unpaired t
660 test; * = $p < 0.05$, ** = $p < 0.01$).

661 **Figure 3. Booster vaccination with NILV::S_{CoV-2} through i.n. route elicits full protection of brain**
662 **from SARS-CoV-2 infection in K18-hACE2^{IP-THV} mice. (A)** Timeline of various NILV::S_{CoV-2}
663 vaccination regimens and SARS-CoV-2 challenge in B6.K18-hACE2^{IP-THV} mice. Immunized mice
664 were set aside for the study of the immune responses without challenge. **(B)** Representative dot plots
665 of IFN- γ response by lung CD8⁺ T cells, after in vitro stimulation with the indicated S_{CoV-2}-derived
666 peptides. **(C)** Cytometric strategy to detect lung CD8⁺ T central memory (T_{cm}, CD44⁺CD62L⁺CD69⁻

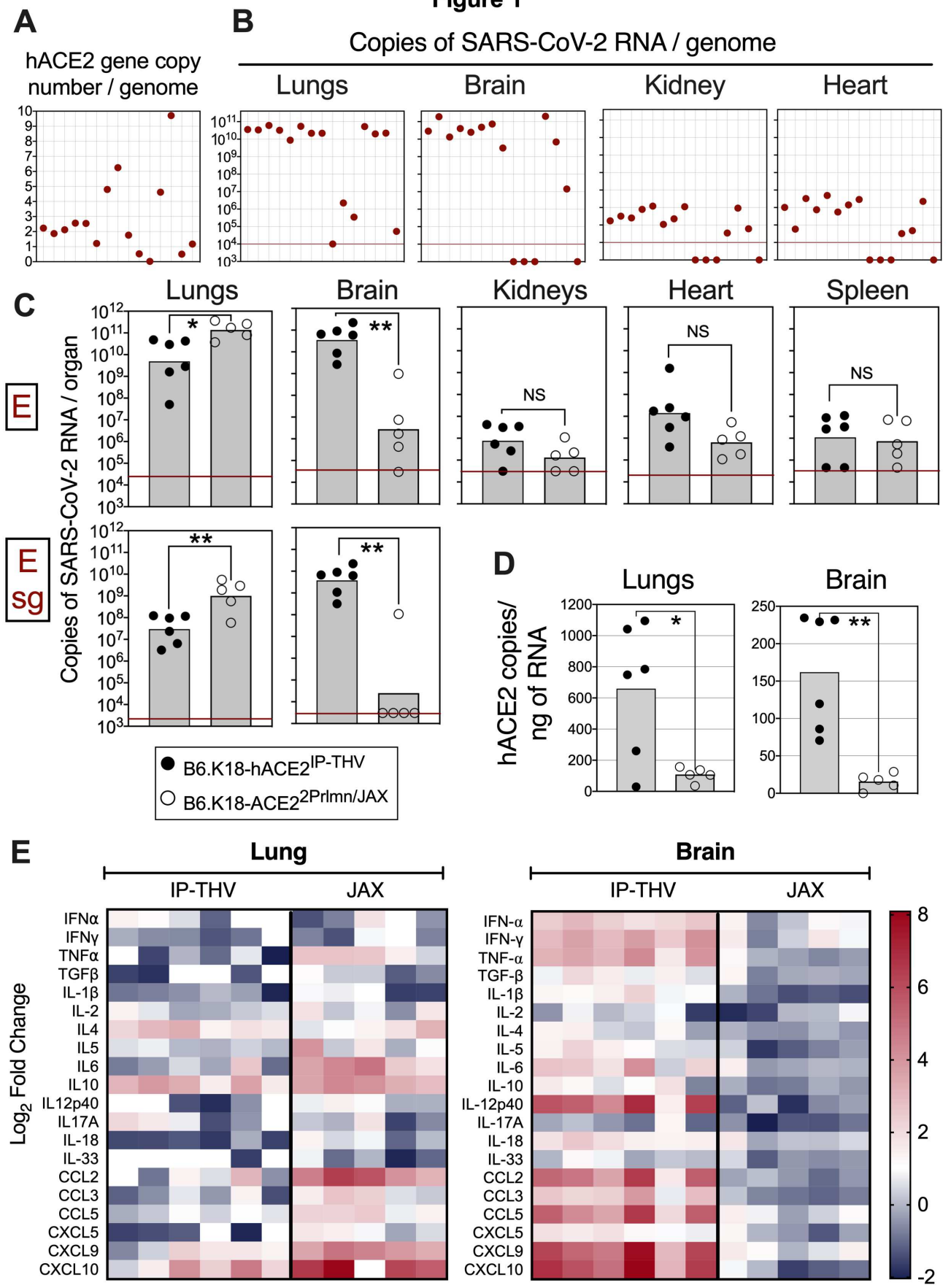
667), T effector memory (Tem, CD44⁺CD62L⁻CD69⁻) and T resident memory (Trm, CD44⁺CD62L⁻
668 CD69⁺CD103⁺) (top) and recapitulative percentages of these subsets in NILV::S_{CoV-2} i.m.-i.n.-
669 vaccinated or sham mice. **(D)** Viral loads in the brain or lungs at 3dpi, determined by conventional E-
670 specific or sub-genomic Esg-specific qRT-PCR. Red lines indicate the qRT-PCR detection limits.
671 Statistical significance of the difference was evaluated by Mann-Whitney test (*= $p < 0.01$).
672 Unexpectedly, one mouse out of the 3 sham-vaccinated mice did not have detectable viral load in the
673 lungs despite a high viral in the brain and hACE2 mRNA expression level comparable to the other
674 mice in the same group. **(E)** Anti-S_{CoV-2} IgG or IgA titers in the sera or lung homogenates at wk 7. **(F)**
675 Serum neutralizing activity (EC50) at wk 7.

676 **Figure 4. Features of olfactory bulbs or brain in the protected NILV::S_{CoV-2}- or unprotected**
677 **sham-vaccinated K18-hACE2^{IP-THV} mice.** Mice are those detailed in the Figure 3. **(A)** CD3 immuno-
678 histo-chemistry of an olfactory bulb from a NILV::S_{CoV-2} i.m.-i.n. vaccinated and protected mice and
679 recapitulative results from this group versus sham-vaccinated and unprotected mice at 3dpi. **(B)**
680 Cytometric analysis of cells extracted from pooled olfactory bulbs from the same groups. **(C-D)** Innate
681 immune cells in the olfactory bulbs **(C)** or brain **(D)**. **(E)** Brain histology at 3 dpi, H&E stain. The top
682 right and both bottom panels show examples, in two different mice, of leukocyte clusters (arrows)
683 alongside the ventricular wall. No such clusters were detected in the NILV::S_{CoV-2} i.m.-i.n. vaccinated
684 mice (top left panel). The close up view (bottom right panel) highlights the thickened, disorganized
685 ependymal lining, compared to the normal ependymal cells and cilia of an NILV::S_{CoV-2} i.m.-i.n.
686 vaccinated mouse (top left panel).

687 **Figure 5. Full protective capacity of NILV::S_{CoV-2} against the Manaus P.1 SARS-CoV-2**
688 **variant.** **(A)** Timeline of NILV::S_{CoV-2} i.m.-i.n. immunization and challenge with Manaus P.1 SARS-
689 CoV-2 in B6.K18-hACE2^{IP-THV} mice. Olfactory bulbs, brains and lungs were collected at 3 dpi. **(B)**
690 Brain or lung viral loads, determined by conventional E-specific or sub-genomic Esg-specific qRT-
691 PCR at 3dpi. Two mice out of the 5 sham-vaccinated mice did not have detectable viral load in the
692 lungs despite a high viral in the brain and hACE2 mRNA expression level comparable to the other
693 mice in the same group. **(C)** Neutralizing activity (EC50) of sera from individual NILV::S_{CoV-2}-
694 vaccinated mice against pseudo-viruses harboring S_{CoV-2} from the ancestral Wuhan strain or D614G,
695 B1.117, B1.351 or P.1 variants. **(D)** Cytometric analysis of CD8⁺ T cells in pooled olfactory bulbs of
696 NILV::S_{CoV-2} i.m.-i.n. vaccinated and protected mice versus sham-vaccinated and unprotected mice.
697 **(E)** Wild type or μ MT KO mice were injected by NILV::S_{CoV-2} or sham following the time line shown
698 in **(A)**, then pretreated with Ad5::hACE2 4 days before the challenge with SARS-CoV-2 Wuhan strain.
699 Lung viral loads were determined at 3dpi. Statistical significance of the differences was evaluated by
700 Mann-Whitney test (*= $p < 0.01$, **= $p < 0.001$, ****= $p < 0.0001$). **(F)** T-splenocyte responses in

701 NILV::S_{CoV-2}-primed and -boosted C57BL/6 WT mice, evaluated by IFN- γ ELISPOT using 15-mer
702 peptides encompassing S_{CoV-2} MHC-I-restricted epitopes.
703

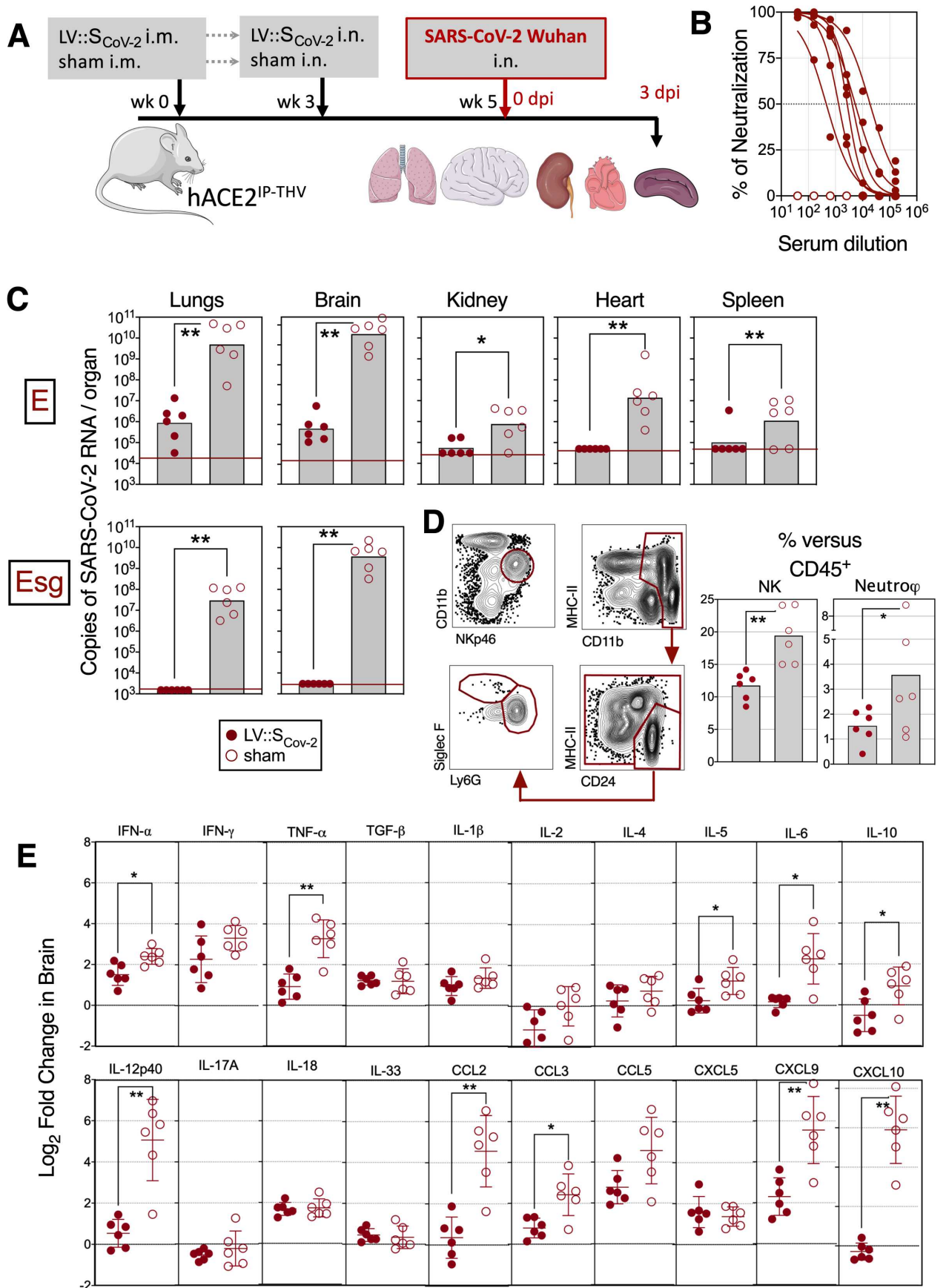
Figure 1



704

705

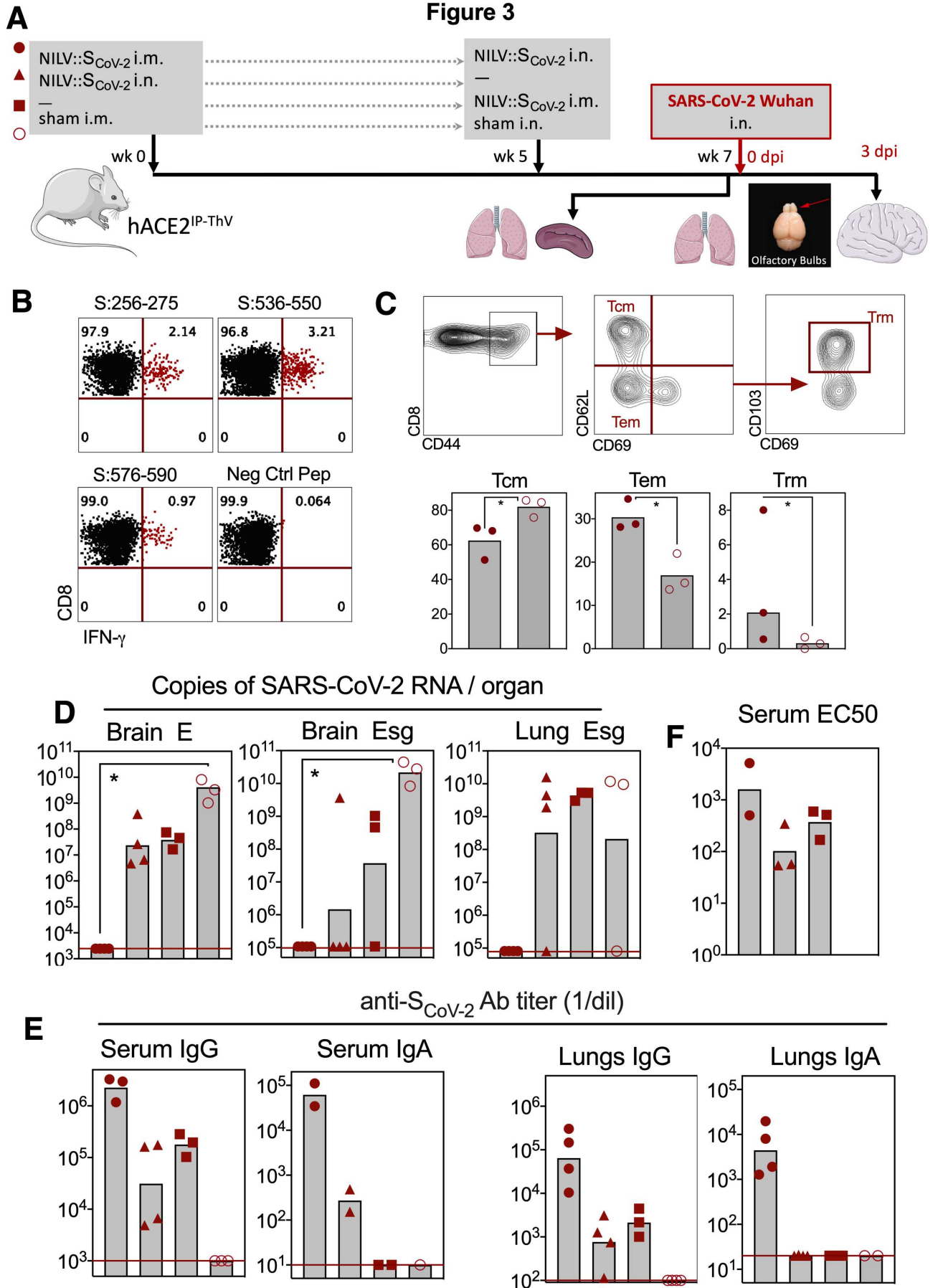
Figure 2



706

707

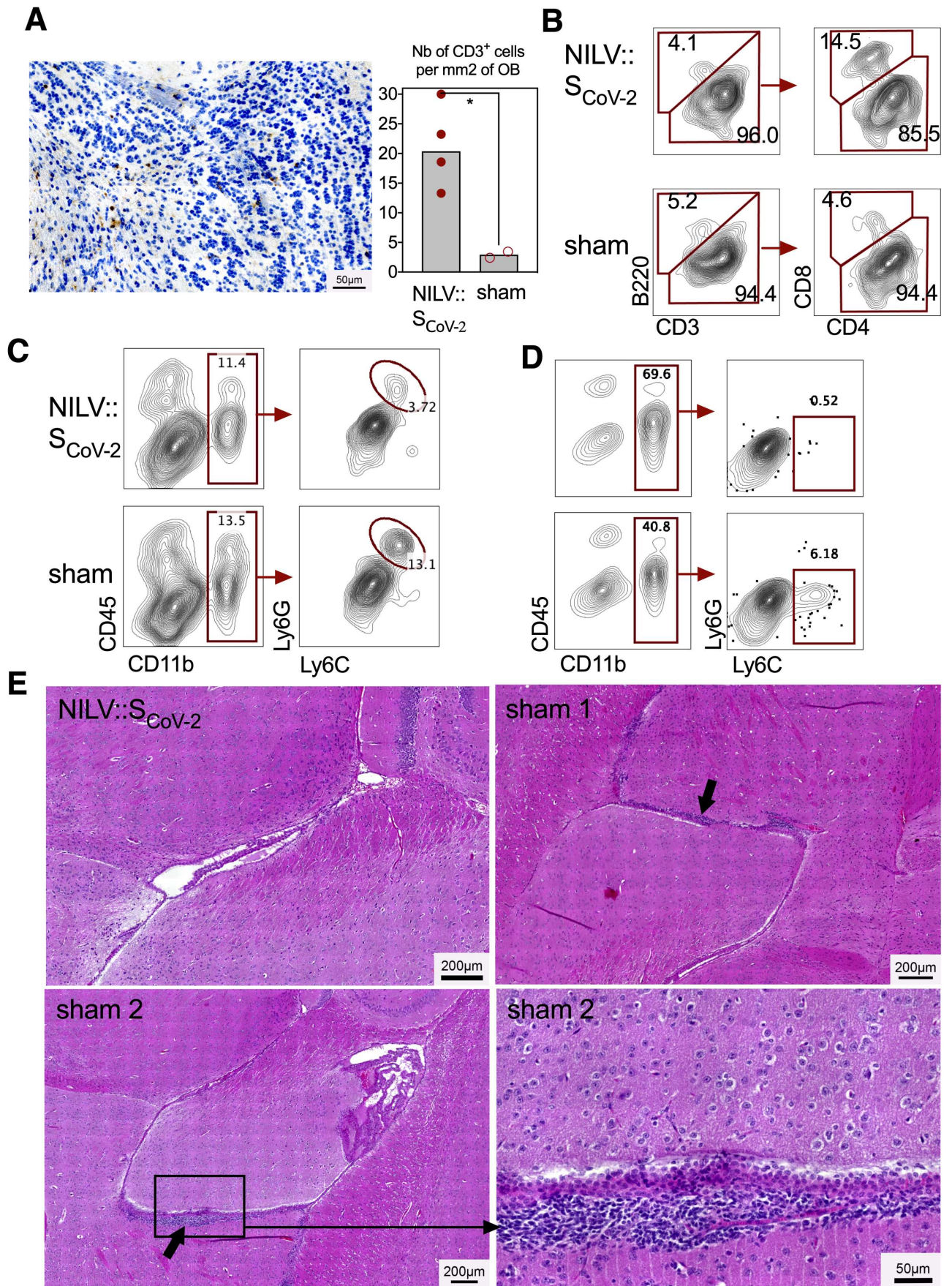
Figure 3



708

709

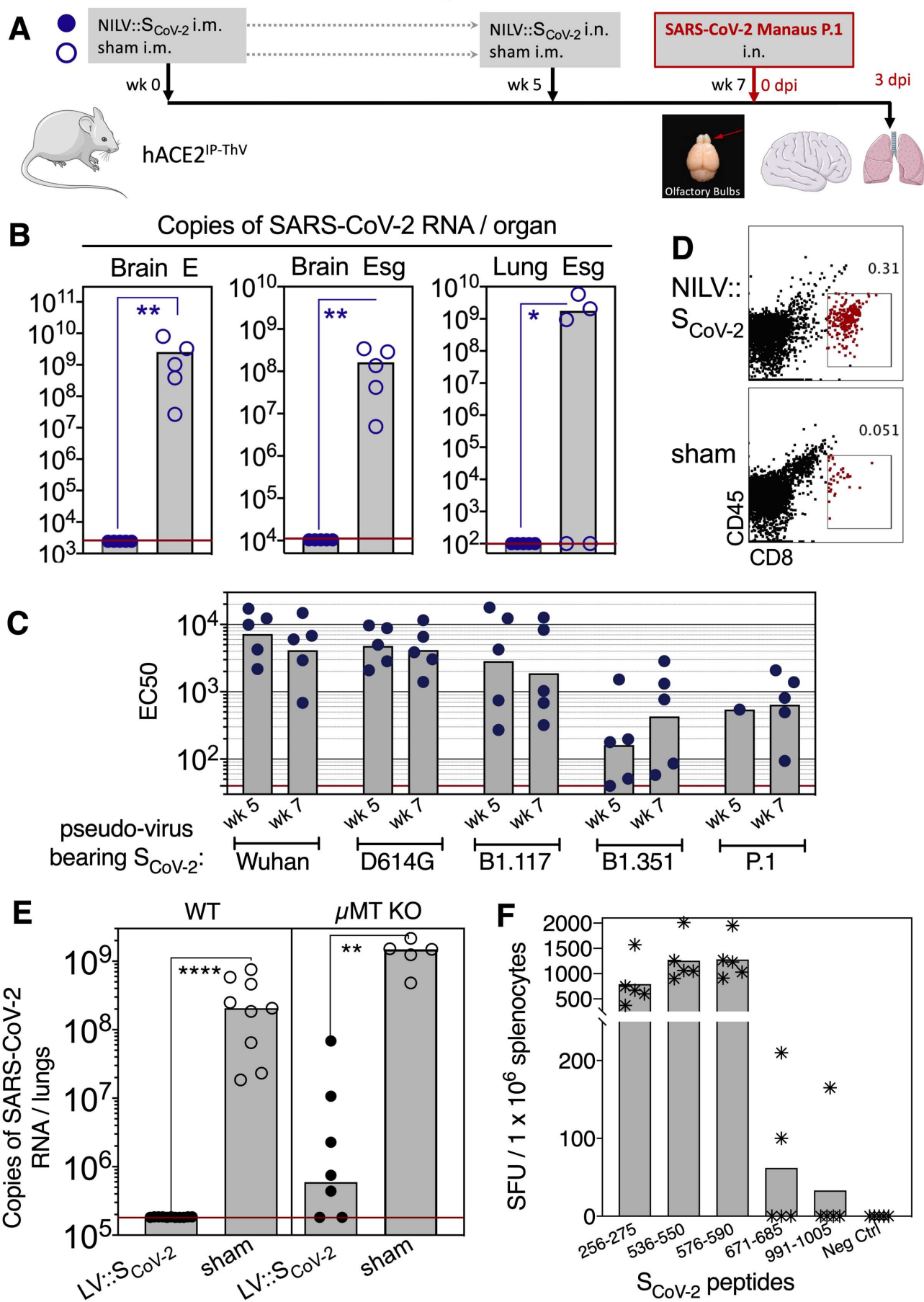
Figure 4



710

711

Figure 5



Figures

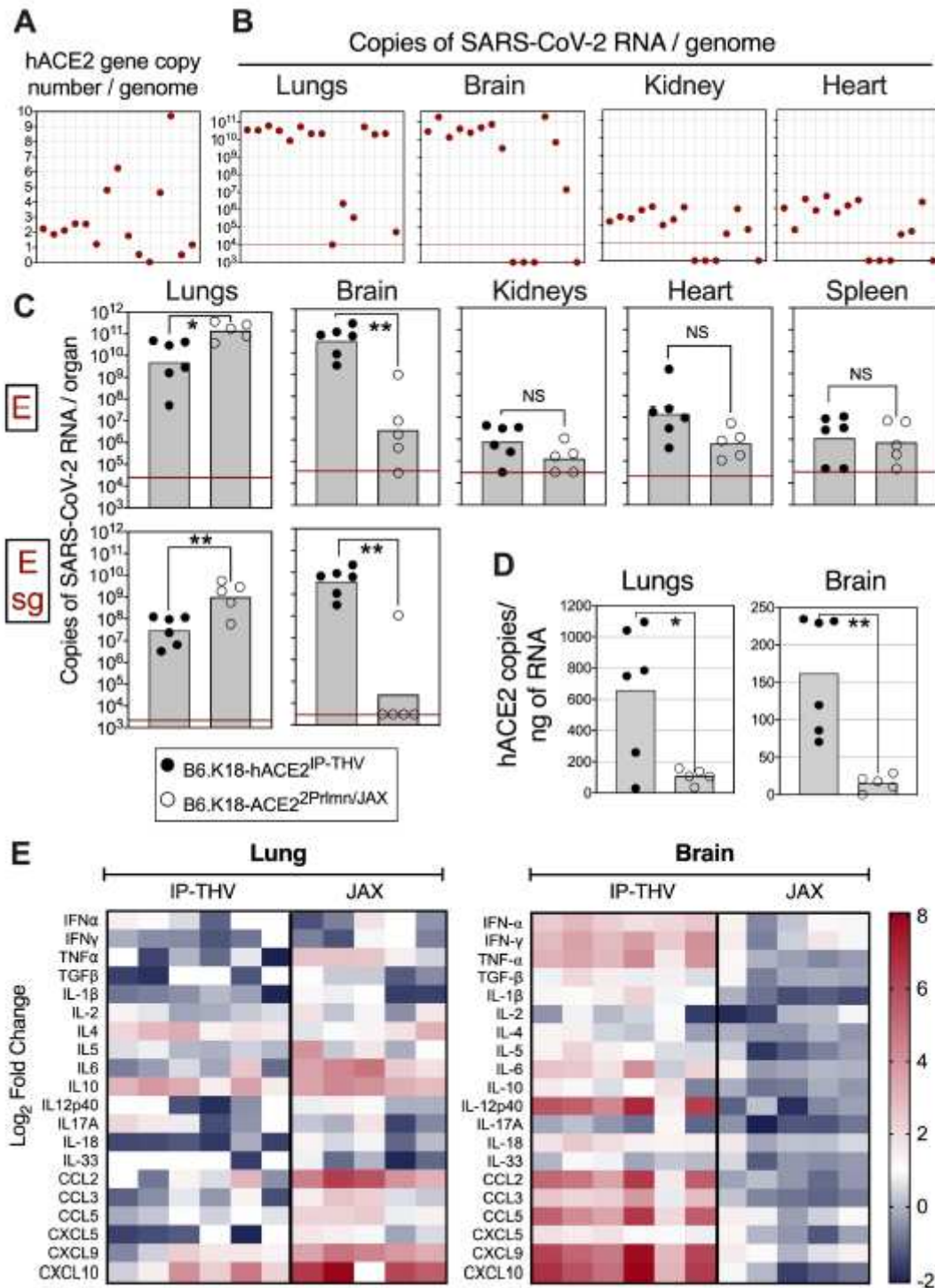


Figure 1

Large permissibility of the lungs and brain of K18-hACE2^{IP-THV} transgenic mice to SARS-CoV-2 replication. (A) Representative genotyping results from 15 N1 B6.K18-hACE2^{IP-THV} mice as performed by qPCR to determine their hACE2 gene copy number per genome. Dots represent individual mice. (B) Phenotyping of the same mice, presented in the same order, inoculated i.n. with 0.3×10^5 TCID₅₀ at the

age of 5-7 wks and viral loads determination in the indicated organs at 3 dpi by conventional E-specific qRT-PCR. (C) Comparative permissibility of various organs from K18-hACE2IP-THV and B6.K18-ACE22PrImn/JAX transgenic mice to SARS-CoV-2 replication, as determined at 3 dpi by conventional E-specific or sub-genomic Esg-specific qRT-PCR. Red lines indicate the qRT PCR limits of detection. Statistical significance of the difference was evaluated by Mann-Whitney test (*= $p < 0.01$, **= $p < 0.00$). (D) Comparative quantitation of hACE-2 mRNA in the lungs and brain of B6.K18-hACE2IP-THV and B6.K18-ACE22PrImn/JAX transgenic mice. (E) Heatmap recapitulating log2 fold change in cytokine and chemokine mRNA expression in the lungs or brain of B6.K18-hACE2IP THV and B6.K18-ACE22PrImn/JAX transgenic mice at 3 dpi. Data were normalized versus untreated controls.

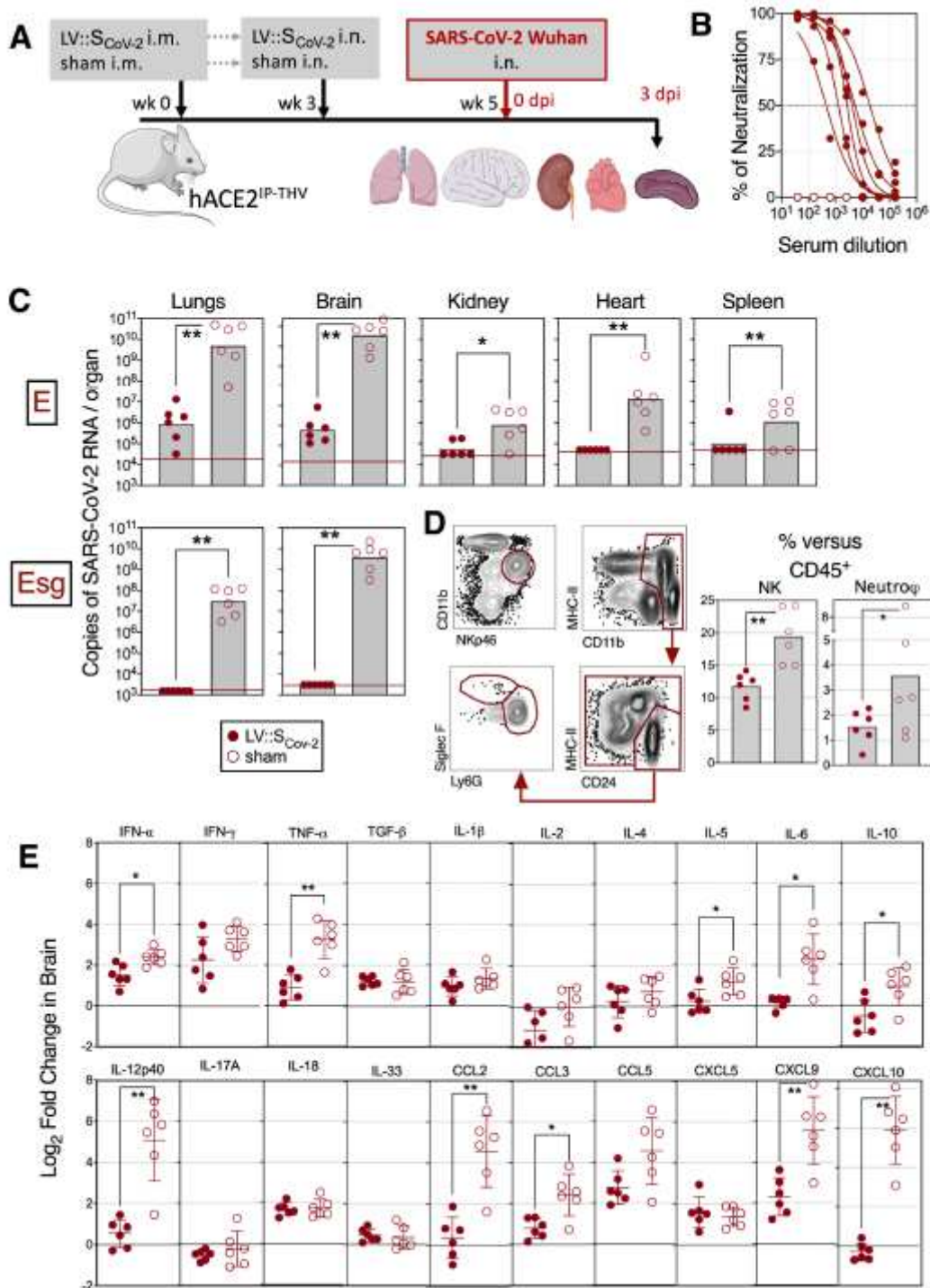


Figure 2

Vaccination with LV::SCoV-2 protects both lungs and central nervous system from SARS-CoV-2 infection in K18-hACE2IP-THV transgenic mice. (A) Timeline of prime-boost LV::SCoV-2 vaccination and SARS-CoV-2 challenge in K18-hACE2IP-THV mice. (B) Serum neutralization capacity of anti-SCoV-2 Abs in LV::SCoV-2-vaccinated mice. (C) Viral loads as determined in various organs at 3dpi by use of conventional E-specific or sub-genomic Esg-specific qRT-PCR. Red lines indicate the qRT-PCR detection limits. Statistical significance of the difference was evaluated by Mann-Whitney test (*= $p < 0.01$, **= $p < 0.001$). (D) Cytometric gating strategy determined to identify and quantify lung NK cells and neutrophils in the lungs of LV::SCoV-2- or sham-vaccinated and SARS-CoV-2-challenged K18-hACE2IP-THV transgenic mice at 3 dpi. Percentages of NK and neutrophil subset were calculated versus total lung CD45+ cells. (E) Relative log₂ fold change in cytokine and chemokine mRNA expression in the brain of LV::SCoV-2- or sham-immunized and SARS CoV-2-challenged K18-hACE2IP-THV transgenic mice at 3 dpi. Means \pm SD are shown. Data were normalized versus untreated controls. Statistical significance was evaluated by two tailed unpaired t test; * = $p < 0.05$, ** = $p < 0.01$).

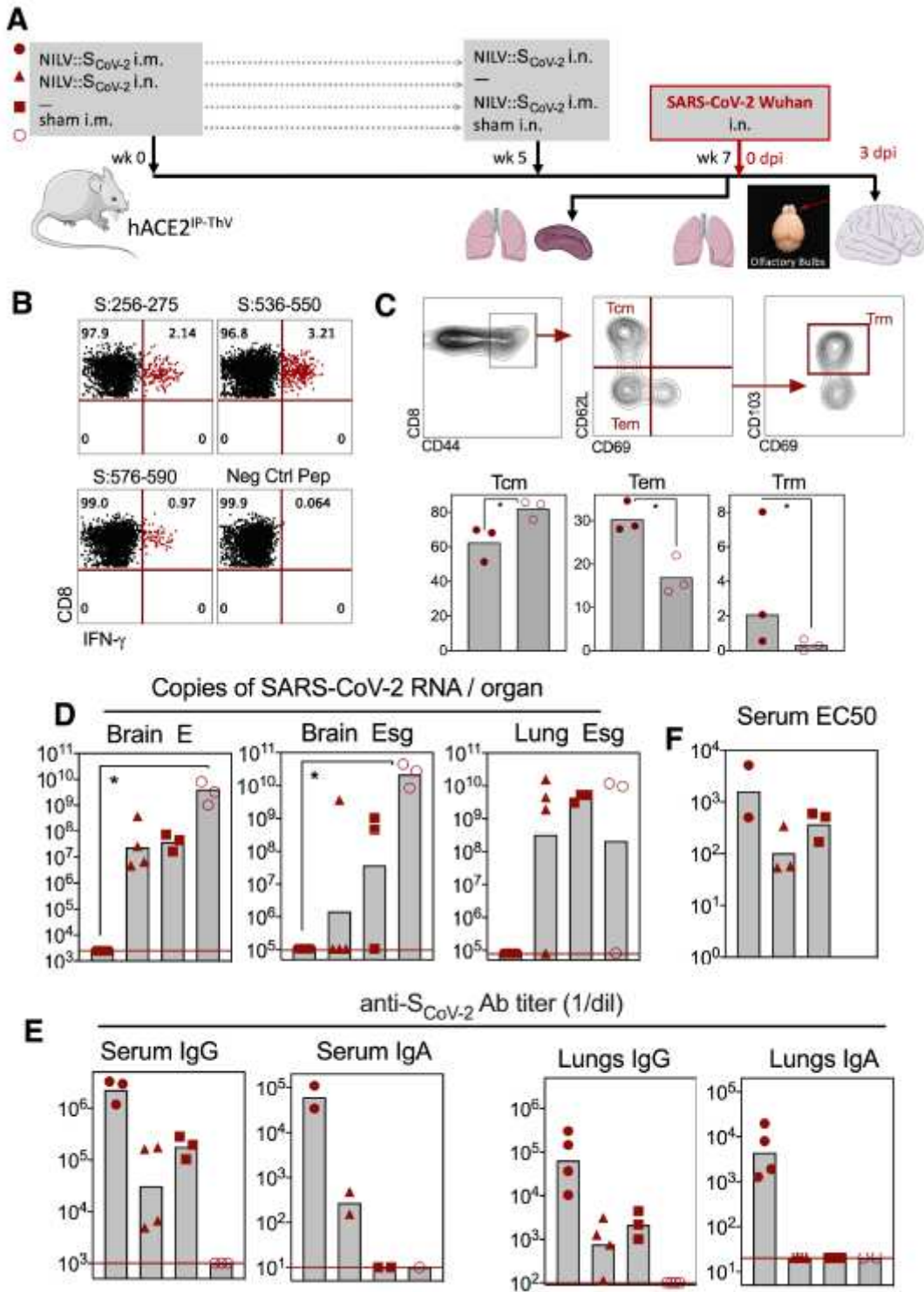


Figure 3

Booster vaccination with NILV::SCoV-2 through i.n. route elicits full protection of brain from SARS-CoV-2 infection in K18-hACE2IP-THV mice. (A) Timeline of various NILV::SCoV-2 vaccination regimens and SARS-CoV-2 challenge in B6.K18-hACE2IP-THV mice. Immunized mice were set aside for the study of the immune responses without challenge. (B) Representative dot plots of IFN-g response by lung CD8⁺ T cells, after in vitro stimulation with the indicated SCoV-2-derived peptides. (C) Cytometric strategy to

detect lung CD8+ T central memory (Tcm, CD44+CD62L+CD69-), T effector memory (Tem, CD44+CD62L-CD69-) and T resident memory (Trm, CD44+CD62L CD69+CD103+) (top) and recapitulative percentages of these subsets in NILV::SCoV-2 i.m.-i.n.- vaccinated or sham mice. (D) Viral loads in the brain or lungs at 3dpi, determined by conventional E specific or sub-genomic Esg-specific qRT-PCR. Red lines indicate the qRT-PCR detection limits. Statistical significance of the difference was evaluated by Mann-Whitney test (*= $p < 0.01$). Unexpectedly, one mouse out of the 3 sham-vaccinated mice did not have detectable viral load in the lungs despite a high viral in the brain and hACE2 mRNA expression level comparable to the other mice in the same group. (E) Anti-SCoV-2 IgG or IgA titers in the sera or lung homogenates at wk 7. (F) Serum neutralizing activity (EC50) at wk 7.

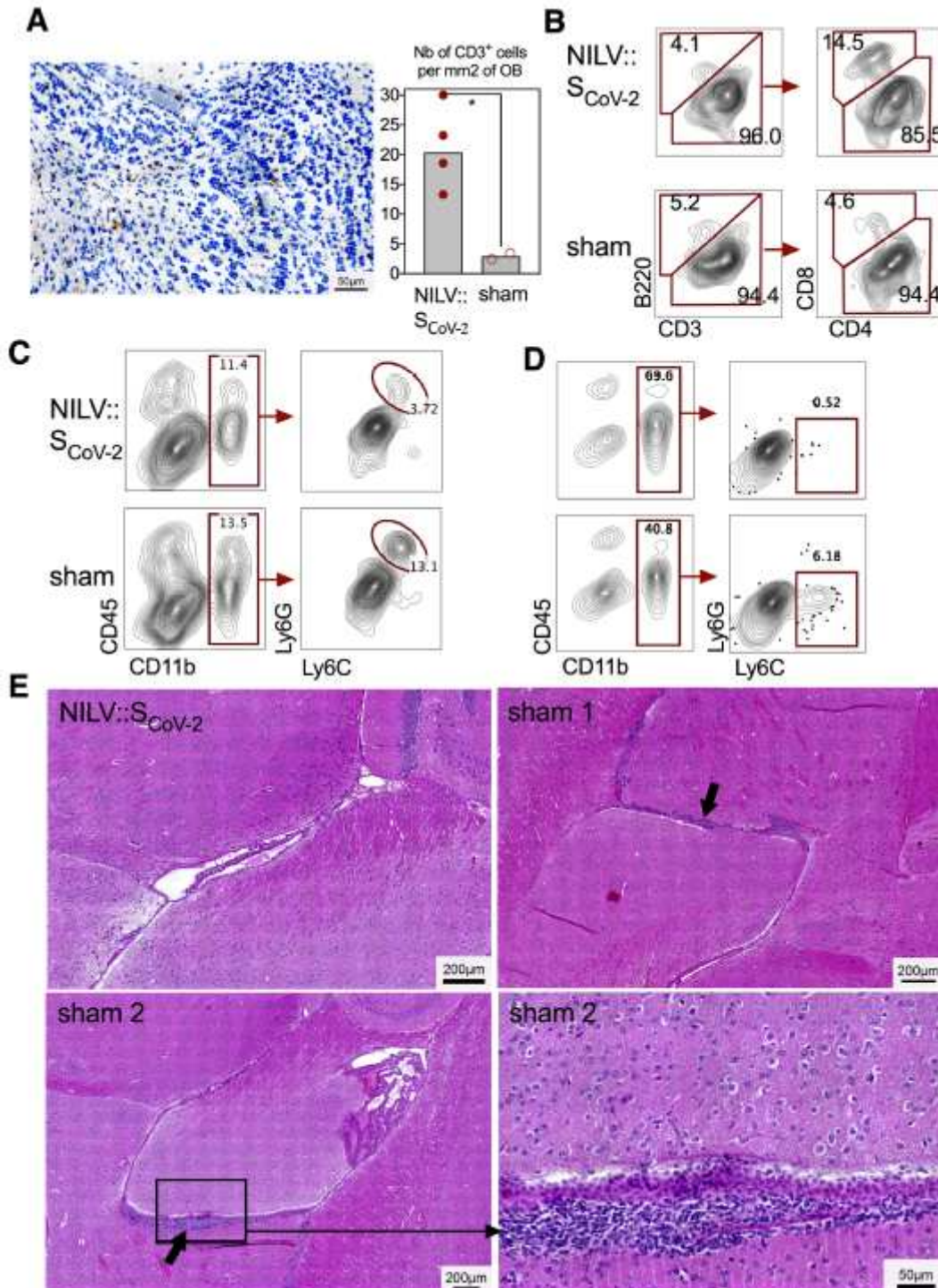


Figure 4

Features of olfactory bulbs or brain in the protected NILV::SCoV-2- or unprotected sham-vaccinated K18-hACE2IP-THV mice. Mice are those detailed in the Figure 3. (A) CD3 immuno histo-chemistry of an olfactory bulb from a NILV::SCoV-2 i.m.-i.n. vaccinated and protected mice and recapitulative results from this group versus sham-vaccinated and unprotected mice at 3dpi. (B) Cytometric analysis of cells extracted from pooled olfactory bulbs from the same groups. (C-D) Innate immune cells in the olfactory bulbs (C) or brain (D). (E) Brain histology at 3 dpi, H&E stain. The top right and both bottom panels show examples, in two different mice, of leukocyte clusters (arrows) alongside the ventricular wall. No such clusters were detected in the NILV::SCoV-2 i.m.-i.n. vaccinated mice (top left panel). The close up view (bottom right panel) highlights the thickened, disorganized ependymal lining, compared to the normal ependymal cells and cilia of an NILV::SCoV-2 i.m.-i.n. vaccinated mouse (top left panel).

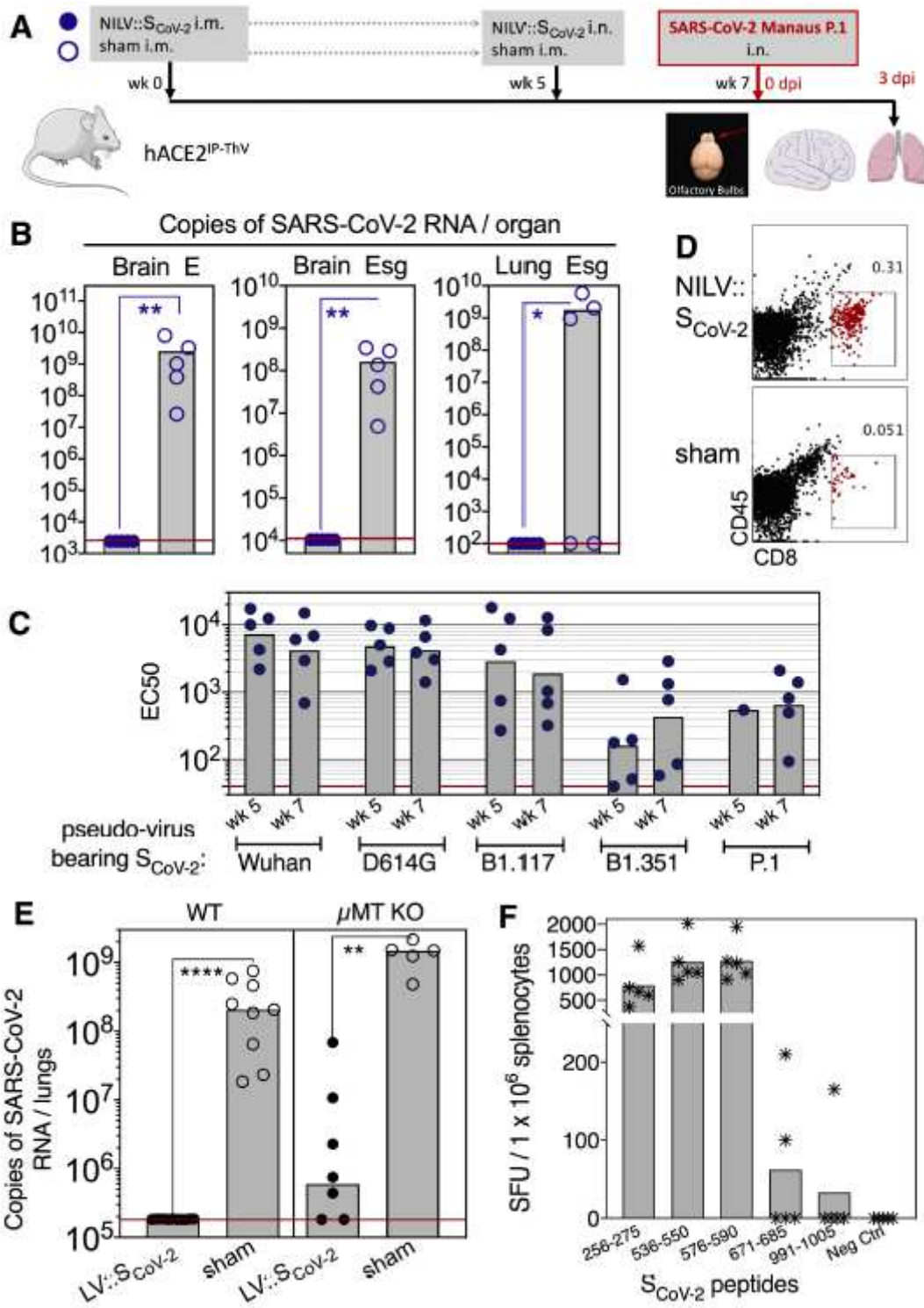


Figure 5

Full protective capacity of NILV::S_{CoV-2} against the Manaus P.1 SARS-CoV-2 variant. (A) Timeline of NILV::S_{CoV-2} i.m.-i.n. immunization and challenge with Manaus P.1 SARS CoV-2 in B6.K18-hACE2^{IP-THV} mice. Olfactory bulbs, brains and lungs were collected at 3 dpi. (B) Brain or lung viral loads, determined by conventional E-specific or sub-genomic Esg-specific qRT PCR at 3dpi. Two mice out of the 5 sham-vaccinated mice did not have detectable viral load in the lungs despite a high viral in the brain and hACE2 mRNA expression level comparable to the other mice in the same group. (C) Neutralizing activity (EC₅₀)

of sera from individual NILV::SCoV-2- vaccinated mice against pseudo-viruses harboring SCoV-2 from the ancestral Wuhan strain or D614G, B1.117, B1.351 or P.1 variants. (D) Cytometric analysis of CD8+ T cells in pooled olfactory bulbs of NILV::SCoV-2 i.m.-i.n. vaccinated and protected mice versus sham-vaccinated and unprotected mice. (E) Wild type or μ MT KO mice were injected by NILV::SCoV-2 or sham following the time line shown in (A), then pretreated with Ad5::hACE2 4 days before the challenge with SARS-CoV-2 Wuhan strain. Lung viral loads were determined at 3dpi. Statistical significance of the differences was evaluated by Mann-Whitney test (*= $p < 0.01$, **= $p < 0.001$, ***= $p < 0.0001$). (F) T-splenocyte responses in NILV::SCoV-2-primed and -boosted C57BL/6 WT mice, evaluated by IFN- γ ELISPOT using 15-mer peptides encompassing SCoV-2 MHC-I-restricted epitopes.

Supplementary Files

This is a list of supplementary files associated with this preprint. Click to download.

- [KuXalSupplNatMicrobiol.pdf](#)